Correspondence to:
M. Asaka,
michinori.asaka@inpex.co.jp

Rock Physics Model of Shale: Predictive Aspect

M. Asaka[1,2] , **R. M. Holt[1]** , **and A. Bakk[3]**

[1]Norwegian University of Science and Technology (NTNU), Trondheim, Norway, [2]INPEX Corporation, Tokyo, Japan, [3]SINTEF, Trondheim, Norway

Abstract Shales often show strong elastic anisotropy that originate from the alignment and platy nature of its constituent minerals. Despite its impact on amplitude variation with offset response and seismic time-shifts, elastic anisotropy of shales is, however, often ignored since it is difficult to measure enough parameters in the field. Being able to correctly estimate anisotropy parameters of shales can therefore significantly improve seismic reservoir characterization. A predictive model is developed by combining existing theories. Properties of locally aligned clay platelets, called domains, are calculated using a rock physics model based on the anisotropic Hashin-Shtrikman estimates. The effect of domain orientation is then accounted for by the orientation distribution function of domains. The applicability of the model was investigated using existing core measurements. Interesting findings include: (a) most of modeled anisotropy parameters are consistent with the measured values even though only limited information was used for the model parameters optimization, and (b) most of optimized interplatelet medium properties are consistent with the saturated fluid and small interplatelet medium shear modulus suggested by existing studies. These findings imply that the model can be used to predict anisotropy parameters from limited information.

Plain Language Summary Shales often show strong elastic anisotropy and it has certain impact on amplitude variation with offset response and seismic time-shifts. Elastic anisotropy of shales is, however, often ignored since it is difficult to measure enough parameters in the field. A predictive rock physics model is developed based on the recently published Sayers-den Boer approach. We show how the model can be used to make realistic estimates of anisotropy parameters based on limited data.

1. Introduction

Most rocks are anisotropic to some extent. The origin of the anisotropy is always heterogeneities on a smaller scale than the volume under investigation, ranging from layered sequences of different rock types down to molecular configurations (Fjær et al., 2008). In particular, shales often show strong elastic anisotropy that originates from the alignment and platy nature of its constituent minerals, as underpinned by laboratory measurements provided by many authors (e.g., Lozovyi & Bauer, 2019; Szewczyk et al., 2018; Vernik & Nur, 1992; Wang, 2002b). It has also been recognized that the elastic anisotropy has impact on seismic imaging (e.g., Thomsen, 1986), amplitude variation with offset (AVO) response (e.g., Blangy, 1994) and seismic time-shifts (e.g., Herwanger & Horne, 2009). For seismic imaging, low-resolution anisotropy parameters are utilized and anisotropic prestack depth migration (PSDM) has become increasingly common. In this case, Thomsen's anisotropy parameter δ (Thomsen, 1986) is estimated from check shot or VSP data and short-spread moveout data. Anisotropy parameter η is found from far-offset moveout, coupled with a correction for ray-bending. Anisotropy parameter ε is subsequently derived from δ and η (Thomsen, 2014). Estimated parameters can however contain errors due to, for example, imperfect decoupling between normal moveout velocity and η. Prior information or geological constraints can therefore improve the velocity model building. High-resolution anisotropy parameters, on the other hand, are necessary for AVO studies and this is often ignored because of our inability to measure sufficient parameters in the field to fully characterize the anisotropic tensor (Bandyopadhyay, 2009). For example, high-resolution parameters can be found from detailed laboratory measurements on cores but such measurements are usually not available especially in nonreservoir interval. In case core material is available, core alteration or damage in addition to difference between in situ and test conditions in terms of stresses, pore pressure, temperature and measurement frequency need to be considered. It is also possible to estimate high-resolution parameters by comparing synthetic seismograms and seismic data AVO responses (Lin & Thomsen, 2013), however, data processing

issues such as incident angle estimate errors and suboptimal prestack offset scaling may result in unusual estimates. Reliable anisotropy parameters estimation method can therefore improve these anisotropic studies.

Scanning electron micrographs of several shales indicate that the shale rocks are comprised of stacks of locally aligned clay platelets (Hornby et al., 1994; Sayers & den Boer, 2019). The stacks are often called domains (Aylmore & Quirk, 1960), and this local alignment is a key source of shale anisotropy (Sayers & den Boer, 2019). Sayers and den Boer (2018) proposed a rock physics model based on the anisotropic Hashin-Shtrikman estimates of Willis (1977) and Ponte Castaneda and Willis (1995). This model, compared to many other rock physics models where the clay platelets in shale are considered to be interconnected (e.g., the differential effective medium scheme [Hornby et al., 1994]), allows the domain to be modeled as anisotropic clay platelets embedded within a soft isotropic interplatelet region. This is an extension of the model proposed by Holt and Fjær (2003), which treats shale rocks as an assembly of isotropic spherical clay particles surrounded by a shell of effective water. The latter model requires an anisotropic add-on (e.g., Bakk et al., 2006), but the anisotropic nature of clay particles can be directly included in the anisotropic Hashin-Shtrikman estimates.

Scanning electron micrography of a shale also indicates that the orientation of domains varies. The effect of the varying orientations on the stiffness can be approximated by weighted averages over all orientations, in which the weighting function is the orientation distribution function (ODF) of domains. Based on the expression that gives the pole density of the platelets as a function of strain (Owens, 1973), the pole density profiles in the case of uniaxial compaction can be expressed using a compaction factor (Baker et al., 1993; Johansen et al., 2004; Ruud et al., 2003). The compaction factor is defined as the ratio between the initial volume and the current volume and can be calculated from the initial porosity and the current porosity if the compaction is solely affected by uniaxial mechanical compaction. Ruud et al. (2003) computed elastic properties of shales using the ODF calculated from compaction factor and domain properties derived from self-consistent approximation.

Various rock physic models for shales have been proposed, but a detailed comparison with laboratory ultrasonic measurements is limited. Vernik and Landis (1996) modified Backus equation (Backus, 1962) using an empirical constant to account for the lateral discontinuity of illite fabric. The modification leads to a better match of the model to ultrasonic velocity measurements (Sayers, 2013b). Ortega et al. (2007) proposed a multi-scale model of shales within the framework of microporomechanics. They found that a unique set of clay mineral stiffness values give reasonable matching to a data set complied from a literature review. Sayers (2013b) demonstrated that the elastic stiffnesses of organic-rich shales can be reasonably described by the anisotropic Hashin-Shtrikman estimates using kerogen as a soft interplatelet region. Sevostianov and Vernik (2021) modeled shale as a multiphase composite containing clay platelets, quartz grains, tetrahedral pores, and pores of concave/oblate shape, based on the Maxwell homogenization scheme. Their illite-dominated clayplatelet's bedding-normal stiffnesses are based on the semiempirical power-law rock physics model (Vernik, 2016; Vernik & Kachanov, 2010), while clay platelet's anisotropy parameters ε and γ are assumed to be the same as muscovite (Vaughan & Guggenheim, 1986). C_{13} of the clay platelet was also assumed to be the same as muscovite, and these assumptions yielded reasonable fit to measured stiffnesses.

In this study, the rock physics model of Sayers and den Boer (2019) is combined with an ODF calculated from the compaction factor (compaction ODF) to obtain elastic stiffnesses of shale. Shales are modeled as transversely isotropic (TI) materials. Domain properties are calculated using the Sayers and den Boer model in which available theoretical calculations for muscovite and ideal kaolinite properties (Militzer et al., 2011) are used. The effect of domain orientation is then taken into account by the compaction ODF. This approach is an extension of Sayers and den Boer (2020) in which the impact of domain orientation is accounted for by two orientation distribution parameters W_{200} and W_{400}; here, those are related by the compaction ODF. This compaction ODF-based model is similar to the existing methods (e.g., Hornby et al., 1994; Ruud et al., 2003; Yurikov et al., 2021), but differs from them in that the domain properties are calculated by the anisotropic Hashin-Shtrikman estimates. The applicability of this model was investigated by using existing core measurements. As a conclusion, these measurements can be reasonably explained by the model, and anisotropy parameters can be estimated from limited information; the prediction power based on limited information makes the model very useful and practical tool for geoscientists.
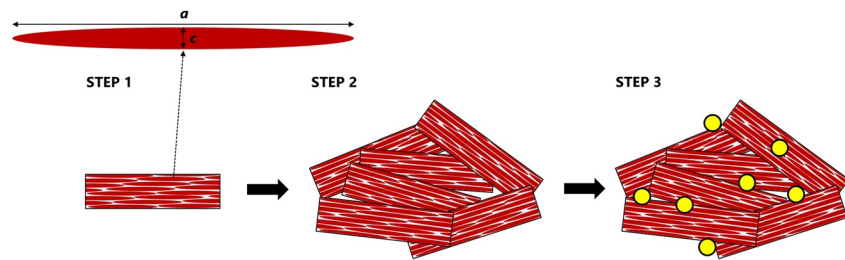
Figure 1. Three-step procedure used to model the shale's properties: (1) compute domain's properties, (2) compute the effect of varying domain orientations, and (3) compute the effect of inclusions of other minerals.

2. Model

Sayers and den Boer (2018) proposed a rock physics model based on the anisotropic Hashin-Shtrikman estimates of Willis (1977) and Ponte Castaneda and Willis (1995). This model is chosen here because (a) it allows the domain to be modeled as anisotropic clay platelets embedded within a soft isotropic interplatelet region; this seems to be a reasonable assumption for shale rocks, and (b) calculations can be performed using a convenient closed-form analytic formulation (Sayers & den Boer, 2019). The model gives a strict lower bound since the matrix (interplatelet region) is the most compliant phase. Sayers (2013b) demonstrated that the elastic properties of organic-rich shales can be reasonably described by this model using elastic stiffnesses of kerogen as a soft interplatelet region. On the other hand, the model assumes that the spatial distribution of clay platelets as defined by a two-point correlation function has the same aspect ratio as the clay platelets (Sayers & den Boer, 2019). This may not be a reasonable assumption for some shale rocks, however, as demonstrated by Ponte Castaneda and Willis (1995), the effect of the spatial distribution of the inclusions on the effective modulus tensor is relatively small. Note that the expression for the effective elastic stiffness tensor in this model can also be derived from Maxwell's homogenization scheme (Maxwell, 1873) extended to a TI medium containing inhomogeneities (Sevostianov, 2014; Sevostianov & Giraud, 2013; Vilchevskaya & Sevostianov, 2015).

Clay platelets are represented as aligned oblate spheroids in the respective domains, which are flattened ellipsoids with equatorial dimension a greater than the polar dimension c (cf. Figure 1). The aspect ratio of these ellipsoidal inclusions is c/a, where c is parallel to the axis of rotational symmetry x_3, and a is parallel to the plane of x_1 and x_2. Thus, the domain's model parameters consist of the elastic stiffness of the pure solid clay mineral, the aspect ratio of clay platelets, the volume fraction of clay platelets, and the bulk and shear moduli of the interplatelet medium (Sayers & den Boer, 2019). Verification of the domain properties calculation was performed by reproducing the results of Sayers (2013b).

Elastic moduli have not been measured experimentally for single crystals of clay minerals, due to technical difficulties associated with their small grain size (Sayers & den Boer, 2020). In this study, a best-fitting TI approximation of theoretical calculations of Militzer et al. (2011) for dry muscovite and ideal kaolinite provided by Sayers and den Boer (2016, 2018) were therefore used for the clay mineral properties (Table 1). Note that muscovite is both structurally and compositionally similar to the clay mineral illite (Katahara, 1996; Tosaya, 1982), and the theoretical calculation are consistent with the available laboratory measurements on muscovite. The volume fraction of clay platelets was calculated from porosity and mineral volume fractions. The complexities of clay dehydration, including its impact on porosity and mineralogy, are discussed in Section 5.1.

The effect of domain orientations on the stiffness can be approximated by weighted averages over all orientations, in which the weighting function is the ODF of domains. Based on the expression that gives the pole density of the platelets as a function of strain (Owens, 1973), Baker et al. (1993) provided the formula for the pole density profiles in the case of uniaxial

Table 1

A Best-Fitting Transversely Isotropic Approximation of Theoretical Calculations of Militzer et al. (2011) for Dry Muscovite and Ideal Kaolinite

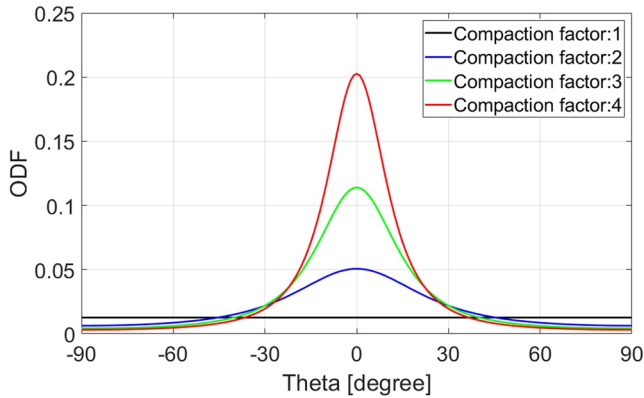|	Muscovite	Ideal kaolinite
C11 (GPa)	181.3	185.9
C13 (GPa)	24.8	5.3
C33 (GPa)	60.1	83.8
C44 (GPa)	20.3	14.8
C66 (GPa)	66.3	58.8
Delta	0.0941	−0.3768
Epsilon	1.0083	0.6092
Gamma	1.1330	1.4865

Figure 2. Compaction orientation distribution function as a function of the angle between the vertical axis and the short axis of clay platelets for four different values of compaction factor α as defined in Equation 1.

compaction. The compaction ODF, which is an ODF as a result of uniaxial compaction, can be expressed as follows using the normalization factor of $1/(8\pi^2)$ (e.g., Bandyopadhyay, 2009; Dutta, 2018):

$$W(\theta) = \frac{1}{8\pi^2} \frac{\alpha^2}{\left(\cos^2\theta + \alpha^2 \sin^2\theta\right)^{\frac{3}{2}}} \tag{1}$$

where θ is the angle between the vertical axis and the short axis of clay platelets. α is a compaction factor defined as the ratio between the initial volume and the current volume (see Equation 4 below). Figure 2 shows the compaction ODF as a function of θ for four different values of the compaction factor. Note that the orientation is assumed to be random before the onset of deformation ($\alpha = 1$), and the compaction ODF for small θ (nearly horizontal clay platelets) increases with an increase in compaction.

The effective elastic properties can be obtained by using the compaction ODF as a weight factor and computing integrals involving tensor rotations (e.g., Dutta, 2018). This procedure is however numerically cumbersome and therefore formulations based on the representation of the ODF in a series of generalized spherical harmonics (Roe, 1965; Sayers, 1994) are commonly used. When the ODF has a vertical rotational symmetry axis, only two coefficients in an expression of the ODF in generalized spherical harmonics, W_{200} and W_{400}, are required to obtain the effective elastic properties (Sayers, 1994):

$$\begin{aligned} W_{200} &= \int_{-1}^{1} W(\xi) Z_{200}(\xi) d\xi \\ W_{400} &= \int_{-1}^{1} W(\xi) Z_{400}(\xi) d\xi \end{aligned} \tag{2}$$

with

$$\begin{aligned} \xi &= \cos\theta \\ Z_{200}(\xi) &= \sqrt{\frac{5}{2}} \frac{3\xi^2 - 1}{2} \\ Z_{400}(\xi) &= \sqrt{\frac{9}{2}} \frac{35\xi^4 - 30\xi^2 + 3}{8} \end{aligned} \tag{3}$$

where $Z_{200}(\xi)$ and $Z_{400}(\xi)$ are called generalized Legendre functions. By using the coefficients W_{200} and W_{400}, the weighted average can be performed by either the Voigt approximation or the Reuss approximation. The elastic stiffness of the shale is obtained by averaging the elastic stiffness tensor over all orientations in the Voigt approximation (Sayers, 1986, 1994), while the elastic compliances of the shale are calculated by averaging the elastic compliance tensor of the domains over all orientations in the Reuss approximation (Sayers, 1987). When domains are isotropic, the elastic stiffness given by the Voigt approximation represents the upper bound while the Reuss approximation gives the lower bound. See Appendix A for the expressions for the Voigt and Reuss approximations. Since the moduli and anisotropy parameters calculated using Voigt and Reuss schemes could be considerably different from each other (Dutta, 2018), the relative proportion within the two averaging schemes is also considered as a free parameter in this study. The relative proportion lies between 0 and 1 (0 coincide with the Reuss scheme while 1 gives the Voigt scheme) although the Voigt and Reuss schemes are not strict bounds for anisotropic domains (e.g., Bayuk et al., 2008). Note that the choice of Voigt versus Reuss averaging scheme would depend on configuration of clay platelets, which is very difficult to assess.

The compaction factor, which is the ratio of the final to the initial layer thickness, can be calculated from the initial porosity Φ_0 (the porosity when the rock components were settling at the sea-floor) and the current porosity Φ if the porosity change is solely caused by uniaxial mechanical compaction (Baker et al., 1993; Ruud et al., 2003):

$$\alpha = \frac{1 - \Phi}{1 - \Phi_0} \tag{4}$$

Table 2
Elastic Properties Assumed for Other Minerals

	Quartz	Calcite	Siderite	Pyrite	K feldspar
Bulk modulus (GPa)	37.5	76.8	123.7	147	37.5
Shear modulus (GPa)	45	32	51	132	15

The initial porosity depends on the shale content V_{sh}. Here we apply an empirical relationship from Fjær et al. (2006):

$$\Phi_0 = 0.369 + 0.535 V_{sh} \tag{5}$$

This empirical relationship is based on correlation between depositional porosity and mean sediment diameter found in data from Shumway (1960). The effective elastic properties of shale can therefore be calculated from the domain properties, porosity and shale content in this case. The assumption that the porosity change is solely caused by uniaxial mechanical compaction is reasonable at least in the early stages of mudstone compaction (Vernik & Anantharamu, 2020). However, the assumption is less likely when the shale porosity is reduced to less than 20%–25%, where the processes of chemical diagenesis become more important (Vernik & Anantharamu, 2020). Recrystallization of clay minerals during the late stages of diagenesis can either enhance or reduce the alignment of clay platelets depending on the stress history. The compaction factor may therefore have to be adjusted. In general, a prediction of a real initial porosity from the model in Equation 5 should be regarded with reservation. In practice, the compaction factor α in Equation 4 used in the distribution function in Equation 1 is tuning the distribution function (Figure 2), where Φ_0 (initial porosity) is chosen as a pragmatic tuning factor (with some link to the physical reality). Vernik and Anantharamu (2020) demonstrated that the ODF given by Equation 1 fits measured pole density orientation data on low porosity shale samples reasonably well by using the compaction factor as the single fitting parameter (note that their formula for the ODF is in slightly different form; their formula uses the inverse of the compaction factor as Z and the normalization factor of $1/(8\pi^2)$ is not included; however, with the normalization factor, their formula gives the same result as Equation 1). In this study, we adopted simple manual adjustment of the initial porosity when necessary; this process will be described later.

The modeling of the shale elastic properties was performed along the three-step procedure similar to Ruud et al. (2003) using the aforementioned methods and described in Figure 1:

1. Compute domain properties
2. Compute the effect of varying domain orientations
3. Compute the effect of inclusions of other minerals such as Quartz and Calcite

The aforementioned extended Maxwell's homogenization scheme was used in step 3 with aspect ratio of 1 (see e.g., Sayers, 2013b for the equations used to perform the calculations). Mineral properties used in step 3 are listed in Table 2. Free parameters in the procedure are as follows:

1. Aspect ratio of clay platelets
2. Bulk modulus of the interplatelet medium
3. Shear modulus of the interplatelet medium
4. Relative proportion within the Voigt and Reuss schemes
5. Initial porosity (if the compaction factor needs to be adjusted)

3. Model Parameters Sensitivity

Model parameters sensitivity was investigated by varying each parameter from the following base case parameters:

1. Aspect ratio of clay platelets: 0.23
2. Bulk modulus of the interplatelet medium: 2.42 GPa
3. Shear modulus of the interplatelet medium: 0.20 GPa
4. Shale content (Vsh): 0.8 (with Quartz content of 0.2)
5. Initial porosity (to determine the compaction factor): 0.8; calculated from Equation 5

The base case parameters for the aspect ratio of the clay platelets and the bulk and shear modulus of the interplatelet medium are based on numerical values derived by Sayers and den Boer (2018). They obtained those parameters by minimizing the difference between predicted domain stiffnesses based on the aforementioned model and measured stiffnesses given by Ulm and coworkers (Ortega et al., 2007; Ulm &
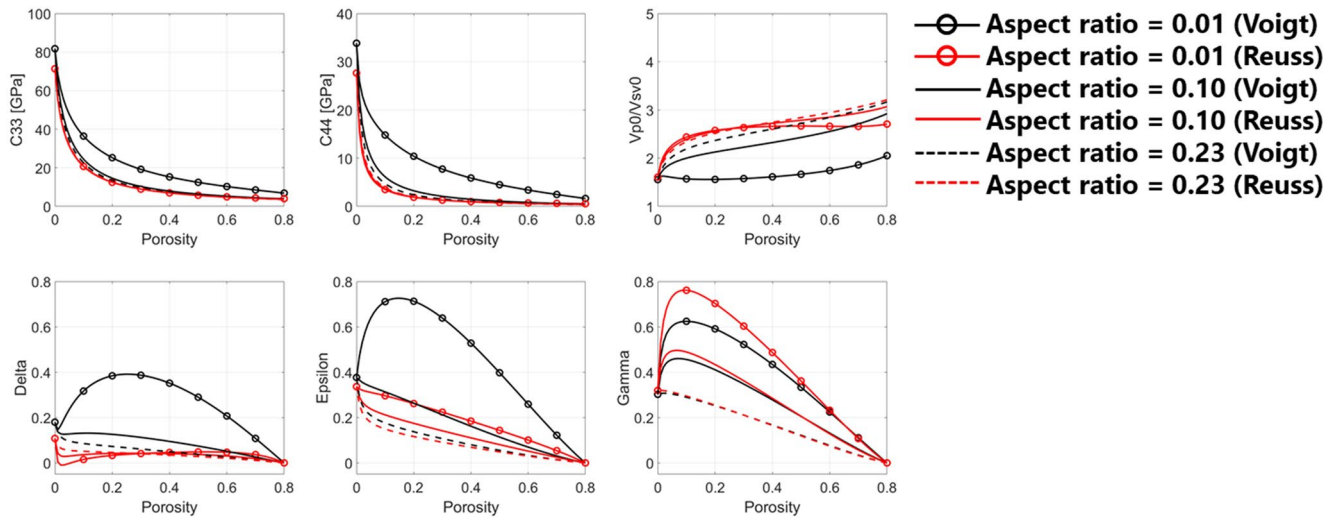
Figure 3. Shale elastic stiffnesses and anisotropy parameters as a function of porosity for three different clay particle aspect ratios for both Voigt and Reuss approximations. The best-fitting transversely isotropic approximation of theoretical calculations for muscovite were used for the clay mineral properties (Table 1).

Abousleiman, 2006). Properties of bound water, which is expected to be a significant ingredient of inter-platelet medium, is discussed by Holt and Kolstø (2017). They performed discrete-element modeling on the molecular scale, and found that normal stiffness for brine confined within ionic layers mimicking a solid clay surface is between 4.2 and 4.5 GPa, whereas shear stiffness is between 0.2 to 0.5 GPa. Although their results stem from 2D simulations with a specific geometry, the results suggest that (a) the crystal-like structure of bound water leads to a nonzero shear modulus, which could be a fraction of 1 GPa, and (b) normal stiffness, which somehow relates to bulk modulus, is of the order and probably larger than that of free water. They also mentioned that water near mineral surfaces may often be highly viscous, as suggested by existing measurements (Antognozzi et al., 2001; Major et al., 2006), so that bound water properties are frequency-dependent. The above aspect ratio of clay platelets (0.23) is higher than typical aspect ratios of between 0.05 and 0.1, and possible explanations for this include: (a) several clay platelets act together as a stack of clay particles, and (b) clay platelets tend to be curved rather than planar (Sayers & den Boer, 2018). The best-fitting TI approximation of theoretical calculations for muscovite were used for the clay mineral properties (Table 1).

Thomsen's anisotropy parameters (Thomsen, 1986) will be used to describe the elastic anisotropy of shale:

$$\varepsilon = \frac{C_{11} - C_{33}}{2C_{33}}$$

$$\gamma = \frac{C_{66} - C_{44}}{2C_{44}}$$

$$\delta = \frac{\left(C_{13} + C_{44}\right)^2 - \left(C_{33} - C_{44}\right)^2}{2C_{33}\left(C_{33} - C_{44}\right)}$$

(6)

3.1. The Aspect Ratio of Clay Platelets

Figure 3 shows shale elastic stiffnesses and Thomsen's anisotropy parameters as a function of porosity with different clay platelets aspect ratio. Results of both Voigt and Reuss averages are given. Key findings for the predicted shale properties based upon the model of Sayers and den Boer (2018) are as follows:

1. C_{33}, C_{44}, and consequently the V_P/V_S velocity ratio ($Vp(0°)/Vsv(0°)$) given by the Reuss average are not sensitive to the aspect ratio.
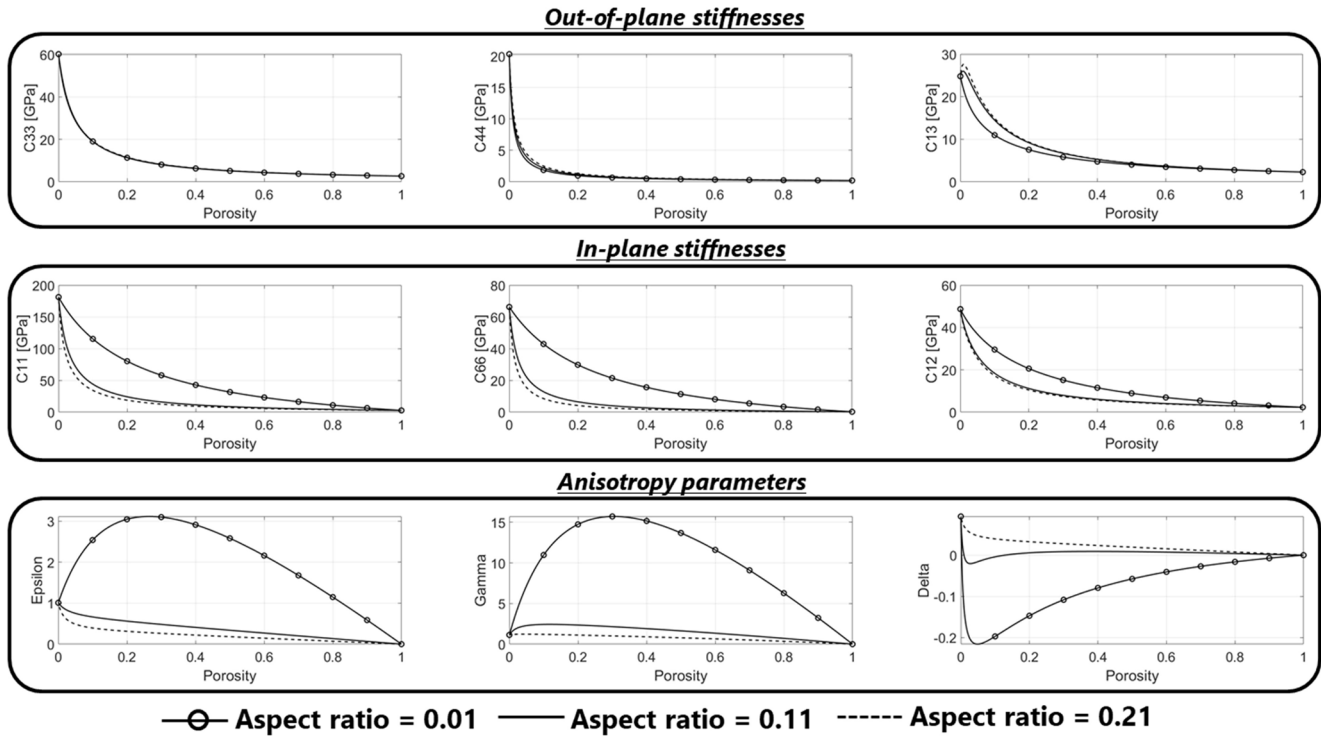
Figure 4. Domain transversely isotropic (TI) elastic stiffnesses and anisotropy parameters as a function of porosity for three different clay particle aspect ratios. Note that porosity is equal to one minus particle (solid) volume fraction. The best-fitting TI approximation of theoretical calculations for muscovite were used for the clay mineral properties (Table 1).

2. C_{33} and C_{44} given by the Voigt average increase with a decrease in the aspect ratio. Since the rate of increase is different between C_{33} and C_{44}, the V_P/V_S velocity ratio decreases with a decrease in the aspect ratio.
3. Anisotropy parameters ε and γ increase with a decrease in the aspect ratio.
4. Separation between the Voigt and Reuss schemes increases with a decrease in the aspect ratio.

The logic behind above findings are: (a) out-of-plane stiffnesses (C_{33} and C_{44}) of domain are not sensitive to the aspect ratio (see Figure 4), (b) in-plane stiffnesses (C_{11} and C_{66}) of domain become significantly larger for small aspect ratio (see Figure 4), (c) domain's out-of-plane stiffnesses are much smaller than domain's in-plane stiffnesses, and (d) the weighted average over the compaction ODF is performed using rotated domain's elastic compliance tensor and elastic stiffness tensor for the Reuss and Voigt approximations, respectively (keep in mind that contributions from small stiffnesses will dominate in the Reuss approximation even if those proportion is small). Changes in separation between the Voigt and Reuss schemes indicate that the relative proportion within two averaging schemes is only an important parameter for small clay platelet aspect ratio.

A comparison of shale anisotropy parameters (Figure 3) with that of domain (Figure 4) shows interesting differences. Thomsen's ε and γ of the shale are significantly smaller than that of the domain, and the shale's δ is almost always positive despite the fact that domain δ has large negative values (see the case with the aspect ratio of 0.01). This is because of the relatively broad domains' orientation. For example, in-plane stiffnesses becomes smaller after the weighted average while out-of-plane stiffnesses becomes larger because of contribution from nonhorizontal domains. This results in smaller ε and γ. Changes in the sign of δ is mainly due to increase in C_{44} and C_{13}, which makes $(C_{13} + C_{44})^2$ larger than $(C_{33} - C_{44})^2$ (see Equation 6).
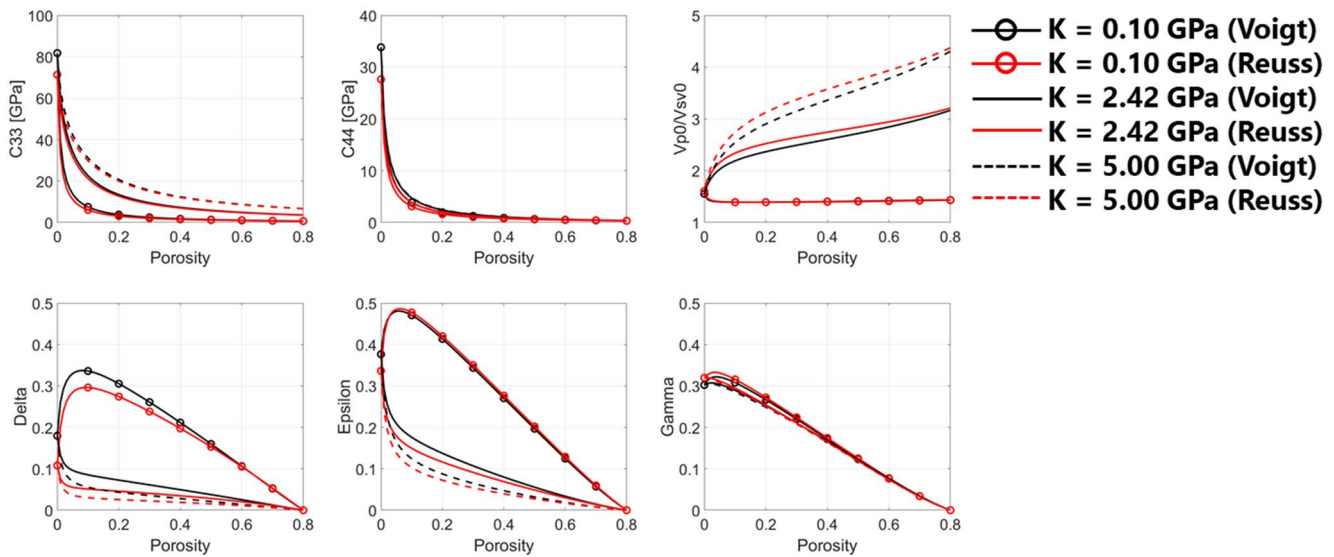
Figure 5. Shale elastic stiffnesses and anisotropy parameters as a function of porosity for three different values of the interplatelet medium bulk modulus.

3.2. The Interplatelet Medium Properties

Figure 5 shows shale elastic stiffnesses and Thomsen's anisotropy parameters as a function of porosity with three different values of the interplatelet medium bulk modulus. Smaller interplatelet medium bulk modulus gives smaller vertical V_P/V_S velocity ratio. This is because smaller interplatelet medium bulk modulus gives smaller C_{33}, while C_{44} is not sensitive to the bulk modulus. This is similar to the fluid impact predicted by the Gassmann's equation (Gassmann, 1951). The anisotropy parameters δ and ε decrease with an increase in the interplatelet medium bulk modulus. This is again similar to the fluid impact predicted by the anisotropic Gassmann's equation (e.g., Mavko & Bandyopadhyay, 2009) in which smaller fluid bulk modulus gives larger anisotropy parameters (e.g., Asaka et al., 2016; Bandyopadhyay, 2009). Anisotropy parameter γ is not sensitive to the interplatelet medium bulk modulus. As a result, ε becomes larger than γ with small interplatelet medium bulk modulus. Note that anisotropy parameters are zero at the initial porosity since the domain orientation is assumed to be random (isotropic) before the onset of deformation.

Figure 6 shows elastic stiffnesses and Thomsen's anisotropy parameters as a function of porosity with three different values of the interplatelet shear modulus. Larger interplatelet shear modulus gives smaller vertical V_P/V_S velocity ratio because it gives larger C_{44} while C_{33} is not sensitive to the interplatelet shear modulus. Anisotropy parameters δ and ε increase with an increase in interplatelet medium shear modulus, which is opposite to the impact of interplatelet medium bulk modulus. Anisotropy parameter γ is not sensitive to the interplatelet shear modulus.

3.3. The Initial Porosity (Compaction Factor)

Figure 7 shows elastic stiffnesses and Thomsen's anisotropy parameters as a function of porosity with three different initial porosities. Changes in the initial porosity gives different strain for a given value of porosity which results in different compaction factor. This is clearly seen for ε and γ. Larger initial porosity gives larger compaction factor which leads to larger ε and γ.

4. Model Versus Experimental Data

For ultrasonic velocities measurements, the accuracy of the calculated anisotropy parameter δ depends on the accuracy of the measurements of the P-wave velocity propagating at an oblique angle to the bedding-normal symmetry axis (e.g., Chichinina & Vernik, 2018; Dellinger & Vernik, 1994; Yan et al., 2018). The confusion between the group and phase velocities arises when relatively large transducers are used. For deviating angles, sufficient small transducers will in practice provide group velocities while phase velocities
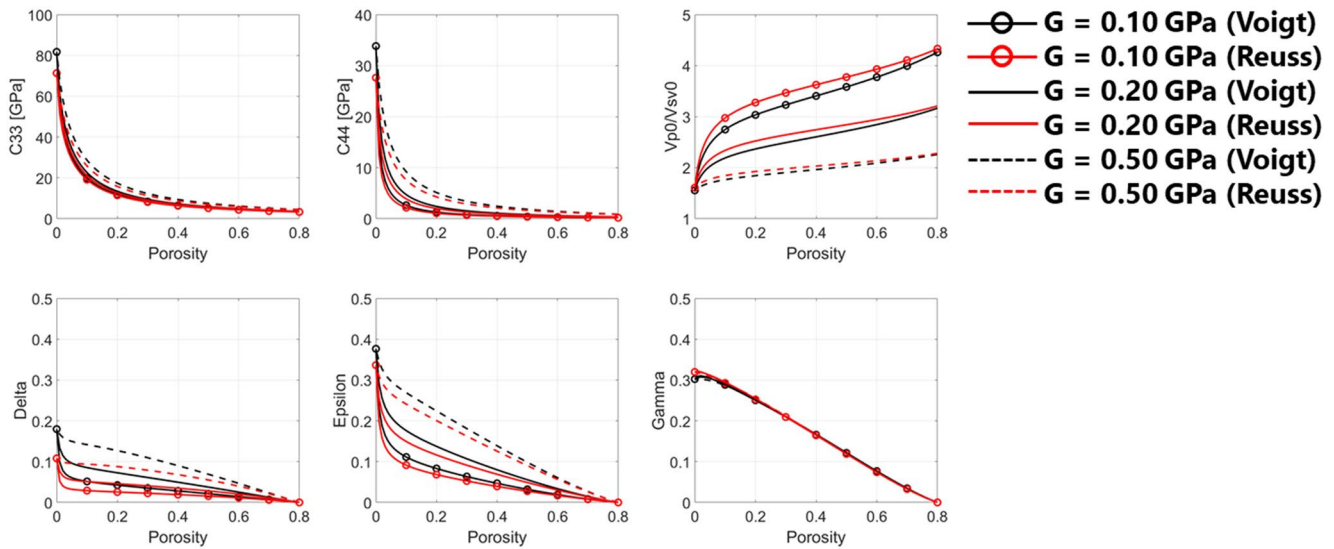
Figure 6. Shale elastic stiffnesses and anisotropy parameters as a function of porosity for three different values of the interplatelet medium shear modulus.

will be obtained with sufficient large transducers (Dellinger & Vernik, 1994). To further increase the accuracy in determination of C_{13} (and δ), multiple oblique velocity measurements on single shale core plugs may be beneficial for reduction of measurement error because of redundancy of measurements, and will also to some degree average out the inevitable inhomogeneities at core scale that otherwise may bias these estimates (Bakk et al., 2020). Single plug measurements ensure consistency in the estimates, and avoid introduction of error when alternatively different plugs with (slightly) different properties are used to estimate velocities at different angles (commonly done with plugs drilled normal, parallel and 45° relative to the bedding plane). Physical constraints on C_{13} have also been proposed for reliable estimation of δ. Holt (2016) derived theoretical bounds on elastic moduli of TI material from the fundamental requirement of positive elastic energy. Yan et al. (2016) gave the physical constrains for a specified type of TI medium which is stiffer along the bedding/layering than the symmetry axis, based on the relationships among Poisson's ratios. Chichinina and Vernik (2018) further tighten the upper bound of C_{13} from Postma's inequality applicable to a thin-layered effective medium composed of kerogen and inorganic phase. The impact of measurement frequency should also be noted. Szewczyk et al. (2018) and Mikhaltsevitch et al. (2021) provided good
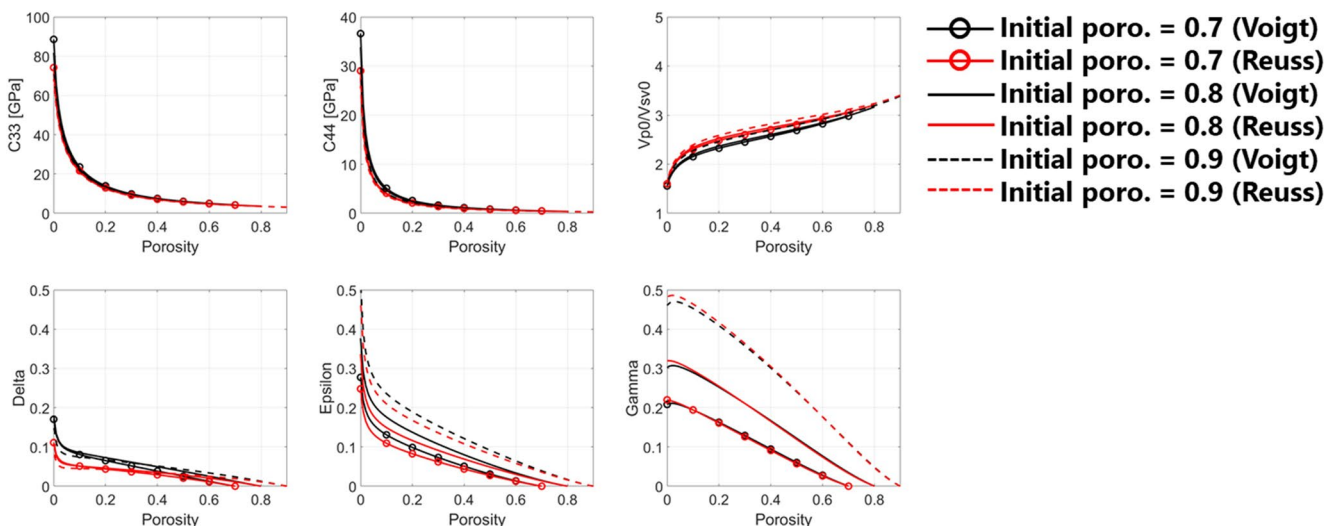

Figure 7. Shale elastic stiffnesses and anisotropy parameters as a function of porosity for three different initial porosities.

Table 3
List of Shale Data Used in This Study

	Porosity	Main mineralogy	Mineralogy used for modeling	Saturation	Applied stress	Measurement
Jurassic shale (outcrop) (Hornby, 1998)	0.085–0.1	Clay: 0.58	Clay (muscovite): 0.69	Water saturated	Isotropic loading	Ultrasonic
		Quartz: 0.31	Quartz: 0.31			
Kimmeridge shale (at 3,750 m) (Hornby, 1998)	0.025	Illite/smectite/mica: 0.35	Clay (muscovite): 0.7	Water saturated	Isotropic loading	Ultrasonic
		Kaolinite: 0.22	Quartz: 0.3			
		Quartz: 0.30				
Shale 2 (Hofmann, 2006)	0.075	Kaolinite: 0.242	Clay (muscovite): 0.6	Brine saturated	Isotropic loading	Low frequency + ultrasonic
		Illite-smectite: 0.134				
		Chlorite: 0.074	Quartz: 0.285			
		Illite and mica: 0.043				
		Quartz: 0.285	Siderite: 0.115			
		Siderite: 0.115				
		K feldspar: 0.054				
Norwegian Sea shale (Dewhurst et al., 2011)	0.14	Kaolinite: 0.52	Clay (ideal kaolinite): 0.66	Brine saturated	Triaxial loading	Ultrasonic
		Mica/illite: 0.1	Quartz: 0.34			
		Quartz: 0.34				
Mancos shale (Sarker & Batzle, 2010)	0.066	Clay: 0.33	Clay (muscovite): 0.44	Decane saturated	Isotropic loading	Low frequency + ultrasonic
		Quartz: 0.39	Quartz: 0.39			
		Carbonate: 0.17	Calcite: 0.17			
Opalinus Clay Shaly facies 3 (Lozovyi & Bauer, 2019)	0.16	Clay: ~0.66	Clay (muscovite): 0.74	Brine saturated	Triaxial loading	Static + ultrasonic
		Quartz: ~0.21	Quartz: 0.21			
		Calcite: ~0.05	Calcite: 0.05			
Opalinus Clay Shaly facies 4 (Lozovyi & Bauer, 2019)	0.16	Clay: ~0.67	Clay (muscovite): 0.75	Brine saturated	Triaxial loading	Static + ultrasonic
		Quartz: ~0.2	Quartz: 0.2			
		Calcite: ~0.05	Calcite: 0.05			
Opalinus Clay Sandy facies 2 (Lozovyi & Bauer, 2019)	0.12	Clay: ~0.42	Clay (muscovite): 0.53	Brine saturated	Triaxial loading	Static + ultrasonic
		Quartz: ~0.39	Quartz: 0.39			
		Calcite: ~0.08	Calcite: 0.08			
Pierre shale (Szewczyk et al., 2018)	0.16	Clay: ~0.42	Clay (muscovite): 0.64	Various water saturation	Triaxial loading	Low frequency + ultrasonic
		Quartz: ~0.3	Quartz: 0.3			
		Carbonate: ~0.06	Calcite: 0.06			
D2 shale (provided by SINTEF Industry AS)	0.285	Illite/smectite mixed layer clay: 0.38	Clay (muscovite): 0.8	Brine saturated	Triaxial loading	Ultrasonic
		Smectite: 0.11				
		Kaolinite: 0.14	Quartz: 0.09			
		Mica and illite: 0.07				
		Quartz: 0.09	K feldspar: 0.11			
		K feldspar: 0.11				

Table 3
Continued

	Porosity	Main mineralogy	Mineralogy used for modeling	Saturation	Applied stress	Measurement
B3 shale (provided by SINTEF Industry AS)	0.244	Illite/smectite mixed layer clay: 0.19	Clay (muscovite): 0.84	Brine saturated	Triaxial loading	Ultrasonic
		Smectite: 0.27				
		Kaolinite: 0.10	Quartz: 0.12			
		Mica and illite: 0.20				
		Quartz: 0.12	Pyrite: 0.04			
		Pyrite: 0.04				
B4 shale (provided by SINTEF Industry AS)	0.147	Illite/smectite mixed layer clay: 0.19	Clay (muscovite): 0.69	Brine saturated	Triaxial loading	Ultrasonic
		Smectite: 0.04				
		Kaolinite: 0.18	Quartz: 0.26			
		Mica and illite: 0.16				
		Quartz: 0.26	K feldspar: 0.05			
		K feldspar: 0.05				

examples where measured Young's modulus of shales strongly depend on frequency. Batzle et al. (2006) and Szewczyk et al. (2018) mention that the squirt-flow type mechanism is a possible cause of observed velocity dispersion.

The experimental data are taken from existing literature and provided by SINTEF Industry AS and listed in Table 3. Some of them are taken from *Mr. Anisotropy* database compiled and analyzed by Horne (2013). Mineralogy is approximated in the modeling process to exclude minerals with minor proportion. Hornby (1998) conducted velocity measurements on three differently oriented plugs. He calculated the relative group propagation angle in a TI medium and confirmed that the phase front is recorded in oblique angle *P*-wave velocity measurements. Hofmann (2006) also conducted velocity measurements on three differently oriented plugs, however, details are not mentioned. Although his oblique *P*-wave velocity measurement may contain errors, it was included in the analysis to use ultrasonic measurement as a benchmark for low frequency measurements (as will be shown later in Figure 11, the low frequency measurements are more or less consistent with the ultrasonic measurement [some differences can be explained by the dispersion]). Note that including the oblique *P*-wave velocity measurement does not significantly affect the final results since it is only one sample and the model parameters were optimized using 21 samples (20 low frequency data sets + 1 ultrasonic data set). Dewhurst et al. (2011) measured group velocities at multiple orientations using a single plug. Phase velocities were determined from the measured group velocities using the methods outlined by Dewhurst and Siggins (2006). Sarker and Batzle (2010) adopted the single plug technique described in Wang (2002a). Their oblique *P*-wave velocity measurement potentially contain errors because it may not comply with the Dellinger and Vernik (1994), however, it was included in the analysis to use it as a benchmark for low frequency measurements (see Figure 13 for a comparison between the ultrasonic and low frequency measurements). Again, including the oblique *P*-wave velocity measurement does not significantly affect the final results since it is only one sample. Lozovyi and Bauer (2019) and Szewczyk et al. (2018) conducted phase velocity measurements on three differently oriented plugs. Data provided by SINTEF Industry AS are based on single plug measurements in which very small transducers were used for the oblique ultrasonic measurements ensuring direct measurements of group velocities, obtained at several oblique angles (Bakk et al., 2020). The group velocities were then converted to the corresponding phase velocities to obtain the complete TI dynamic stiffness parameters.
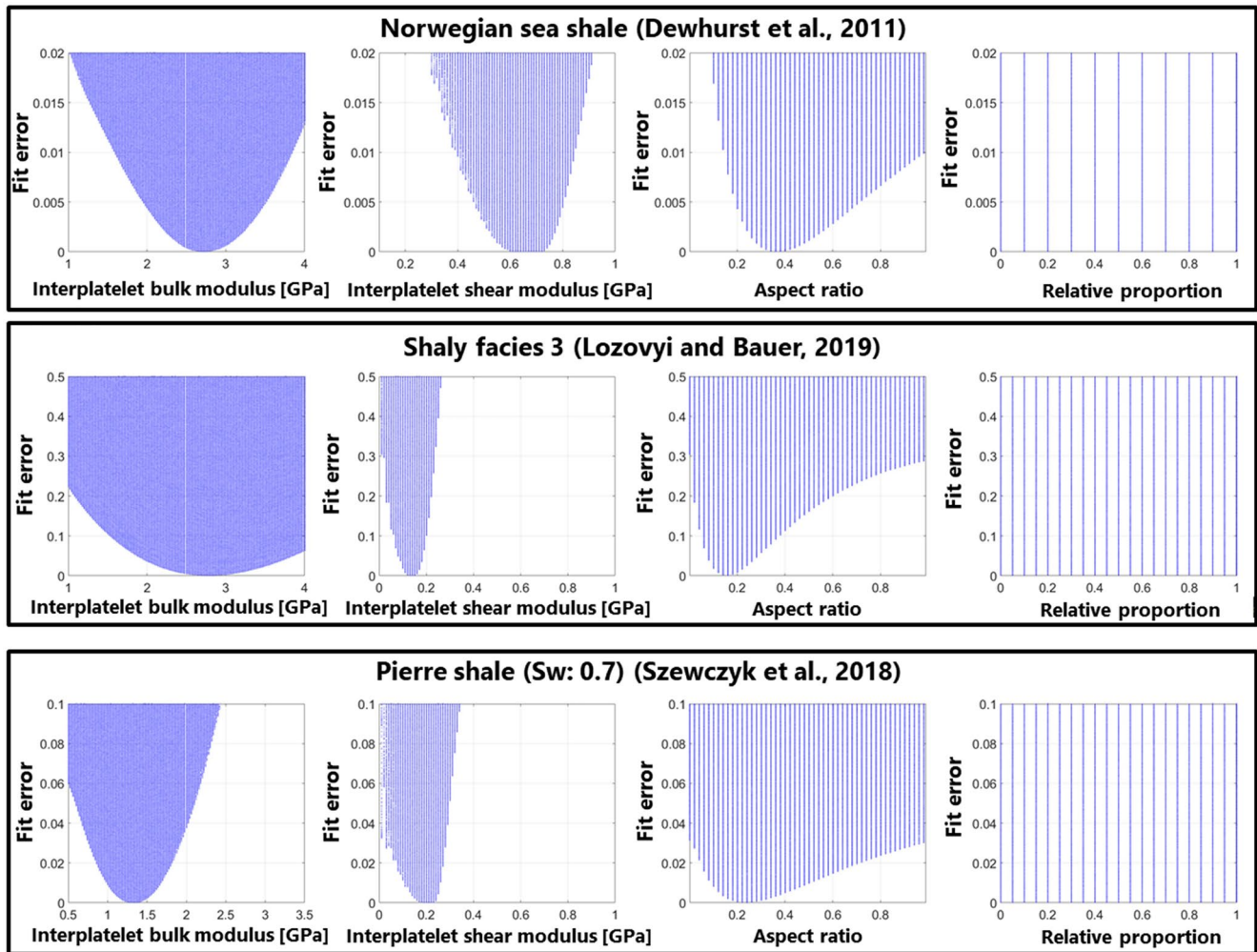
Figure 8. The normalized fit error as a function of model parameters for three samples with the realizations plotted as blue points representing the possible combinations of model parameters (interplatelet medium bulk/shear modulus, aspect ratio, and the relative proportion of bounds) that were searched.

To investigate the applicability of the aforementioned model, model parameters were optimized using measured C_{33}, C_{44}, and C_{66}, which can be measured in field using sonic tools, and the model with the optimized parameters was compared with the measured stiffness and anisotropy parameters. A brute-force grid search was adopted except for the initial porosity with the following search range:

1. The aspect ratio of clay platelets: 0–1
2. The bulk modulus of the interplatelet medium: 0.01–4.00 GPa
3. The shear modulus of the interplatelet medium: 0.01–1.00 GPa
4. The relative proportion within the Voigt and Reuss schemes (0 coincides with the Reuss scheme while 1 gives the Voigt scheme): 0–1

The grid search of coarse intervals was first performed, followed by the second grid search with fine grid and limited search range. The search range for the second grid search was optimized based on the results of the initial grid search. For example, about 114,000 realizations were tested in the second grid search for Jurassic shale sample provided by Hornby (1998).

The best-fitting TI approximation of theoretical calculations for Muscovite were used for the clay mineral properties except for Norwegian Sea shale (Dewhurst et al., 2011), whose dominant clay mineral is kaolinite. The best-fitting TI approximation of ideal kaolinite was used for this shale. Furthermore, Poisson's

Table 4
Optimized Model Parameters and Estimated Brine Bulk Modulus for Each Sample

	Model parameters					Estimated brine bulk modulus (GPa)
	Clay platelets properties	Clay platelets aspect ratio	Interplatelet medium bulk modulus (GPa)	Interplatelet medium shear modulus (GPa)	Initial porosity	
Jurassic shale (Hornby, 1998)	Muscovite	0.05	2.73	0.22	0.74	
Kimmeridge shale (Hornby, 1998)	Muscovite	0.01	1.00	0.11	0.74	
Shale 2 (Hofmann, 2006)	Muscovite	0.03	1.43	0.18	0.8 (adjusted)	
Norwegian sea shale (Dewhurst et al., 2011)	Ideal kaolinite	0.52	2.56	0.83	0.72	2.4
Mancos shale (Sarker & Batzle, 2010)	Muscovite	0.34	0.72	0.38	0.6	
Opalinus Clay Shaly facies 3 (Lozovyi & Bauer, 2019)	Muscovite	0.13	2.67	0.13	0.95 (adjusted)	2.3
Opalinus Clay Shaly facies 4 (Lozovyi & Bauer, 2019)	Muscovite	0.03	2.38	0.14	0.77	2.3
Opalinus Clay Sandy facies 2 (Lozovyi & Bauer, 2019)	Muscovite	0.01	2.75	0.06	0.8 (adjusted)	2.3
Pierre shale (Sw: 0.10) (Szewczyk et al., 2018)	Muscovite	0.15	0.34	0.46	0.71	
Pierre shale (Sw: 0.23) (Szewczyk et al., 2018)	Muscovite	0.14	0.35	0.49	0.71	
Pierre shale (Sw: 0.48) (Szewczyk et al., 2018)	Muscovite	0.23	0.48	0.54	0.71	
Pierre shale (Sw: 0.70) (Szewczyk et al., 2018)	Muscovite	0.19	1.53	0.37	0.71	
D2 shale (SINTEF Industry AS)	Muscovite	0.25	3.30	0.26	0.8	2.6
B3 shale (SINTEF Industry AS)	Muscovite	0.15	3.20	0.34	0.82	3.0 and 3.1
B4 shale (SINTEF Industry AS)	Muscovite	0.05	4.50	0.36	0.74	3.0

ratio of the interplatelet medium was assumed to be positive, which excluded combinations of the bulk and shear modulus resulting in the negative Poisson's ratio. This assumption was adopted by Sayers and den Boer (2020) in their shale modeling study since the interplatelet medium is expected to have properties similar to water. The grid search was performed to minimize the following normalized fit error E:
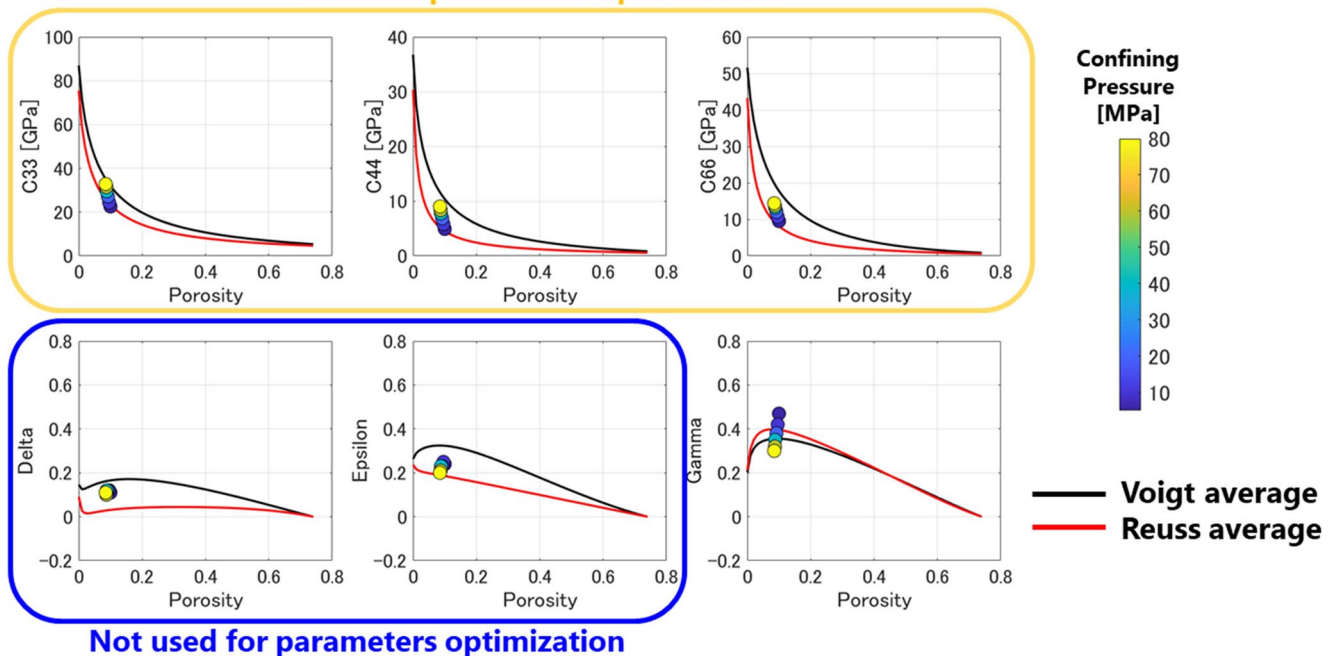

Figure 9. A comparison between optimized model (solid lines) and measurements (circle) on Jurassic shale sample provided by Hornby (1998).
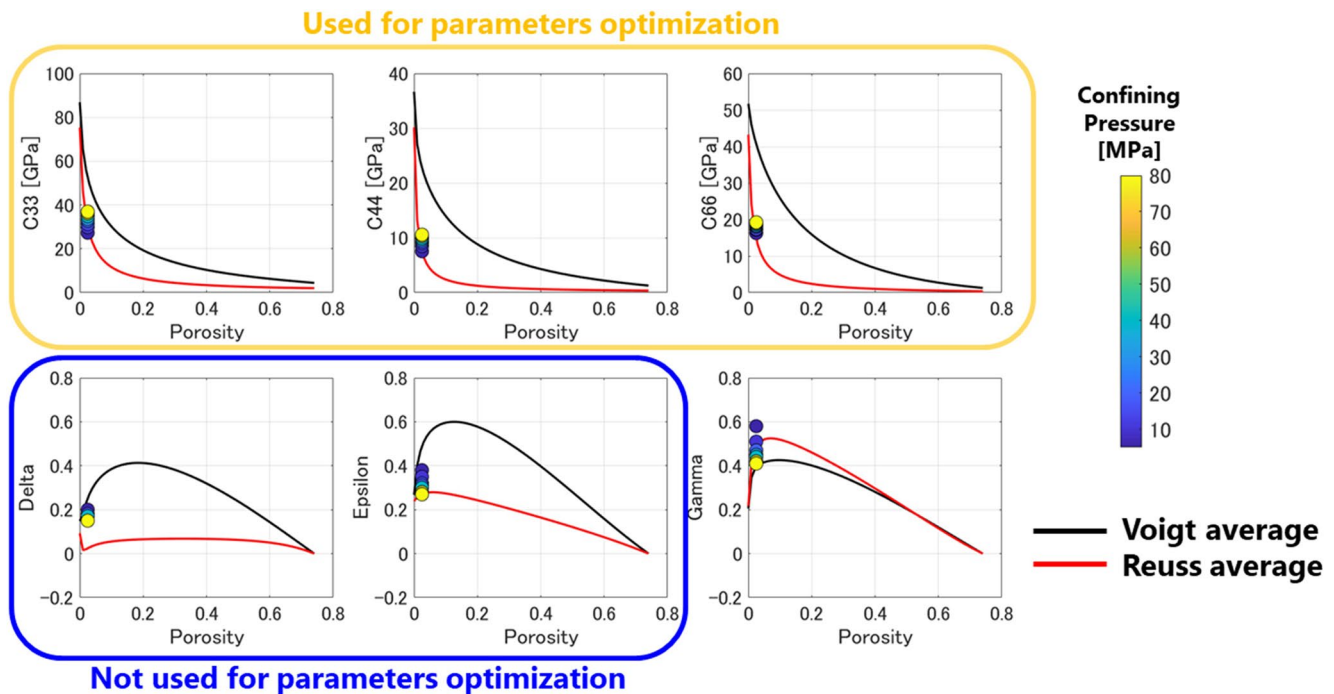
Figure 10. A comparison between optimized model (solid lines) and measurements (circle) on Kimmeridge shale sample provided by Hornby (1998).

$$E = \frac{\left(C_{33}^{\text{mes}} - C_{33}^{\text{mod}}\right)^2}{\left(C_{33}^{\text{mes}}\right)^2} + \frac{\left(C_{44}^{\text{mes}} - C_{44}^{\text{mod}}\right)^2}{\left(C_{44}^{\text{mes}}\right)^2} + \frac{\left(C_{66}^{\text{mes}} - C_{66}^{\text{mod}}\right)^2}{\left(C_{66}^{\text{mes}}\right)^2} \tag{7}$$

where C_{ij}^{mes} and C_{ij}^{mod} are measured and modeled stiffnesses, respectively. The initial porosity was calculated using Equation 5, and it was subsequently adjusted manually for some samples to improve the visual matching between modeled and measured stiffnesses. The manual adjustment is a relatively simple process in which the initial porosity was increased when the modeled anisotropy parameter γ is smaller than the measured one (notice that γ is a function of C_{44} and C_{66}, and it increases with an increase in the initial porosity as shown in Figure 7).

To see the robustness of the grid search, the normalized fit error was calculated for all tested parameter combinations and plotted as a function of one model parameter. The results for three samples are shown in Figure 8, where the realizations are plotted as blue points (each blue point represents the possible combination of model parameters that were searched). Three parameters, interplatelet medium bulk and shear moduli and clay platelets aspect ratio, show a narrow valley, indicating that the optimized parameters have small uncertainty. The relative proportion of the Voigt and Reuss schemes shows a flat valley in these cases. This is because the separation between the two averaging schemes is negligible except for the case with very small clay platelet aspect ratio as shown previously in Figure 3. Note that measurements for each shale were conducted at various pressures or frequencies. Model parameters were therefore first optimized for each pressure or frequency and then averaged to obtain representative parameters for each shale.

The representative parameters and fluid bulk modulus estimated from known temperature, pressure and salinity using Batzle and Wang equations (Batzle & Wang, 1992) are listed in Table 4. Figures 9–18 show a comparison between optimized model and measurements for Jurassic shale sample provided by Hornby (1998), Kimmeridge shale sample provided by Hornby (1998), a shale sample ("Shale 2") provided by
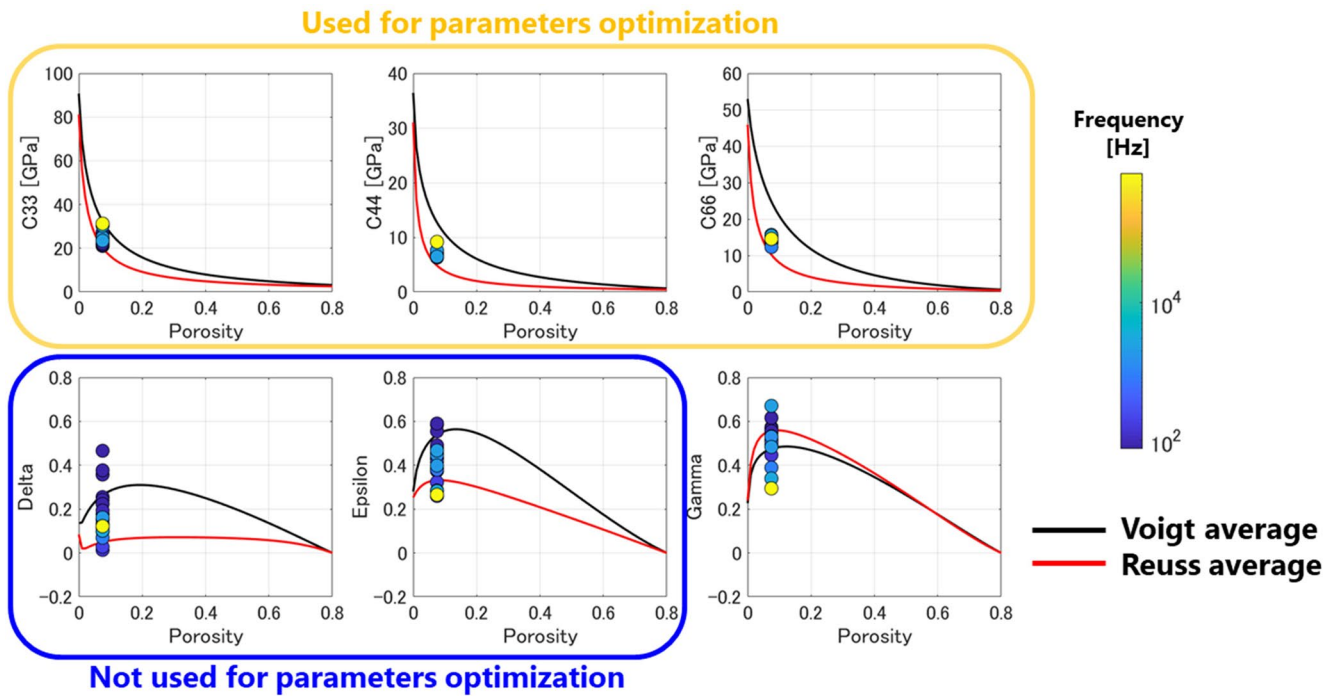
Figure 11. A comparison between optimized model (solid lines) and measurements (circle) on shale sample ("Shale 2") provided by Hofmann (2006).
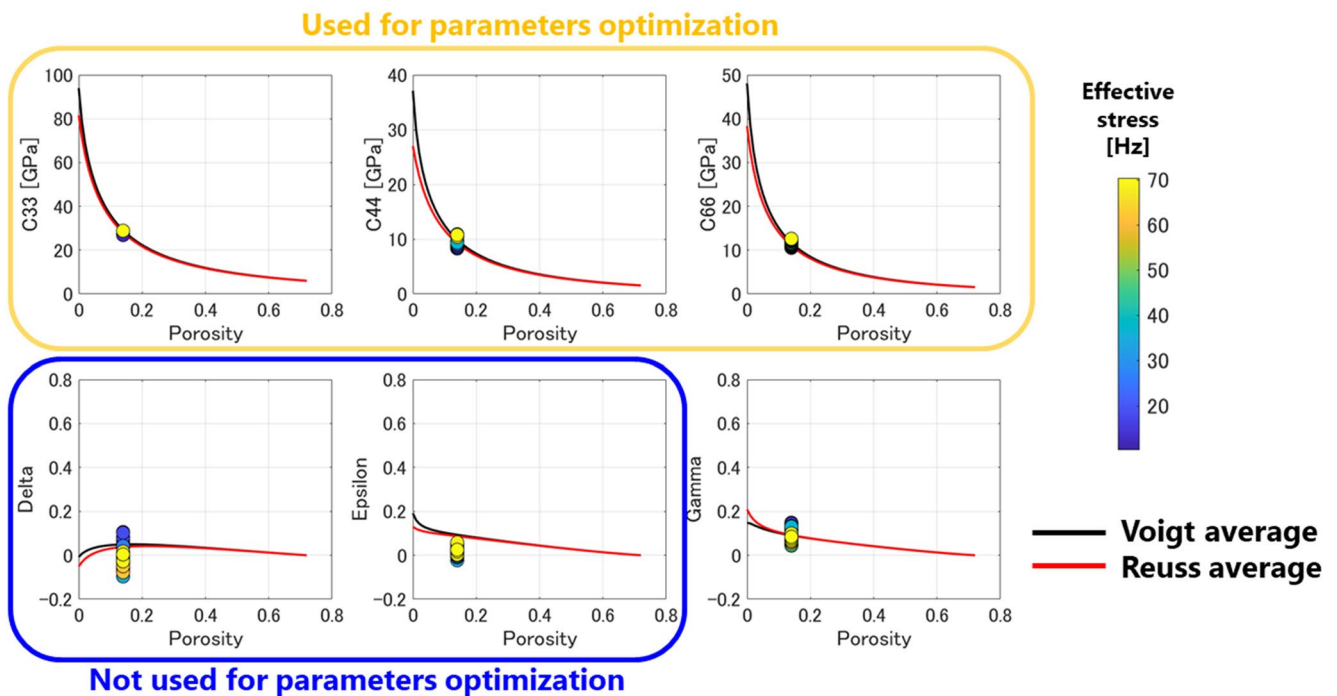

Figure 12. A comparison between optimized model (solid lines) and measurements (circle) on Norwegian Sea shale sample provided by Dewhurst et al. (2011).
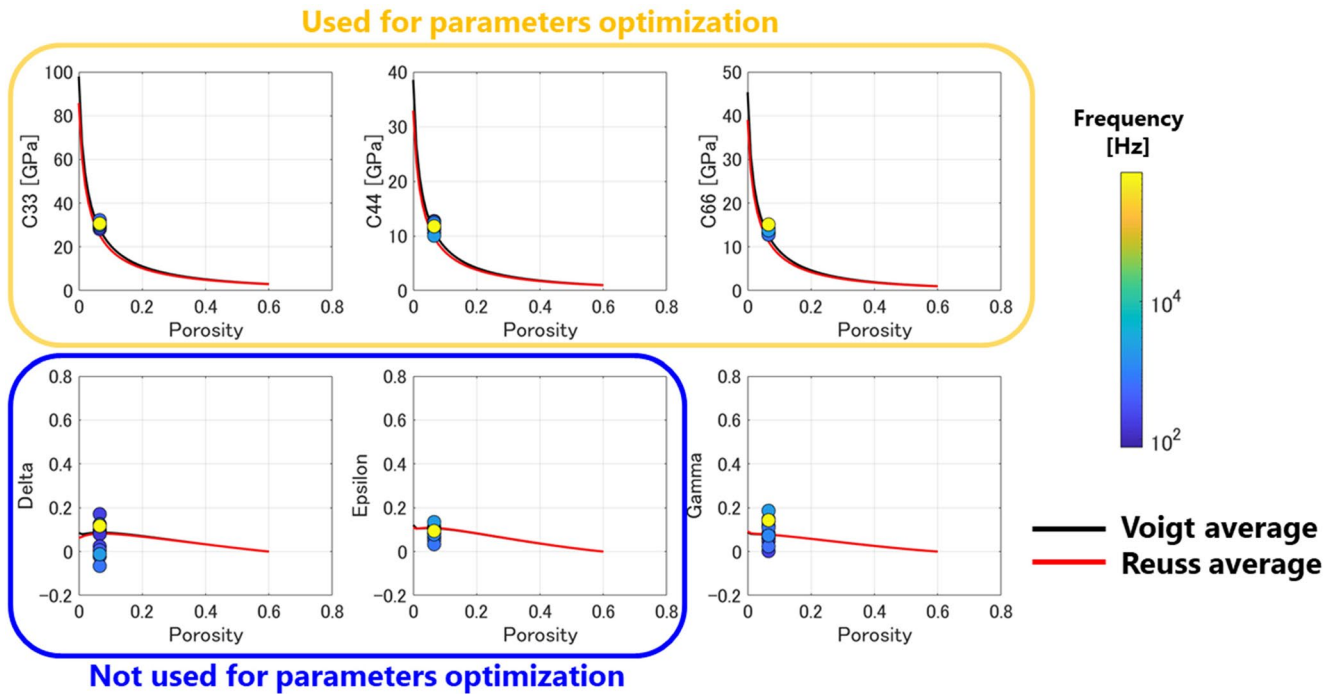
Figure 13. A comparison between optimized model (solid lines) and measurements (circle) on Mancos shale sample provided by Sarker and Batzle (2010).
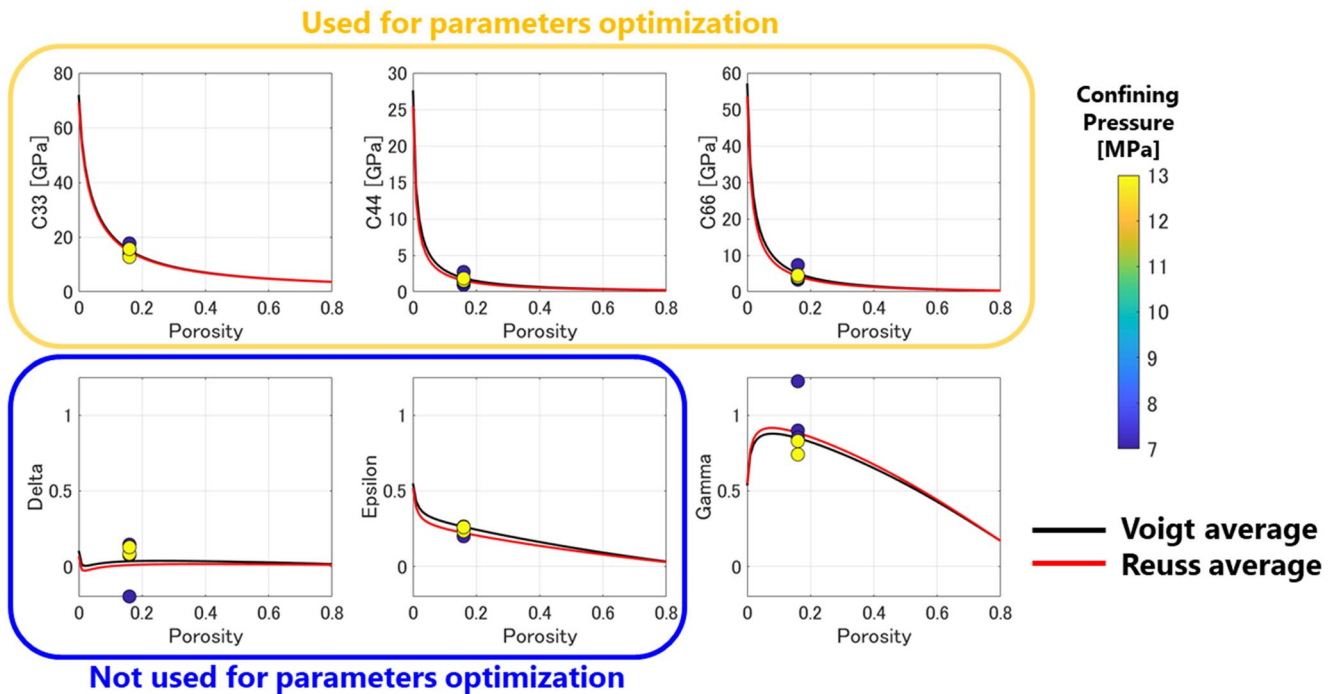

Figure 14. A comparison between optimized model (solid lines) and measurements (circle) on Opalinus Clay sample ("Shaly facies 3") provided by Lozovyi and Bauer (2019). Note that three different measurement results are shown; (1) static undrained stiffness, (2) zero-stress extrapolated static undrained stiffness, and (3) dynamic stiffness based on ultrasonic velocity.
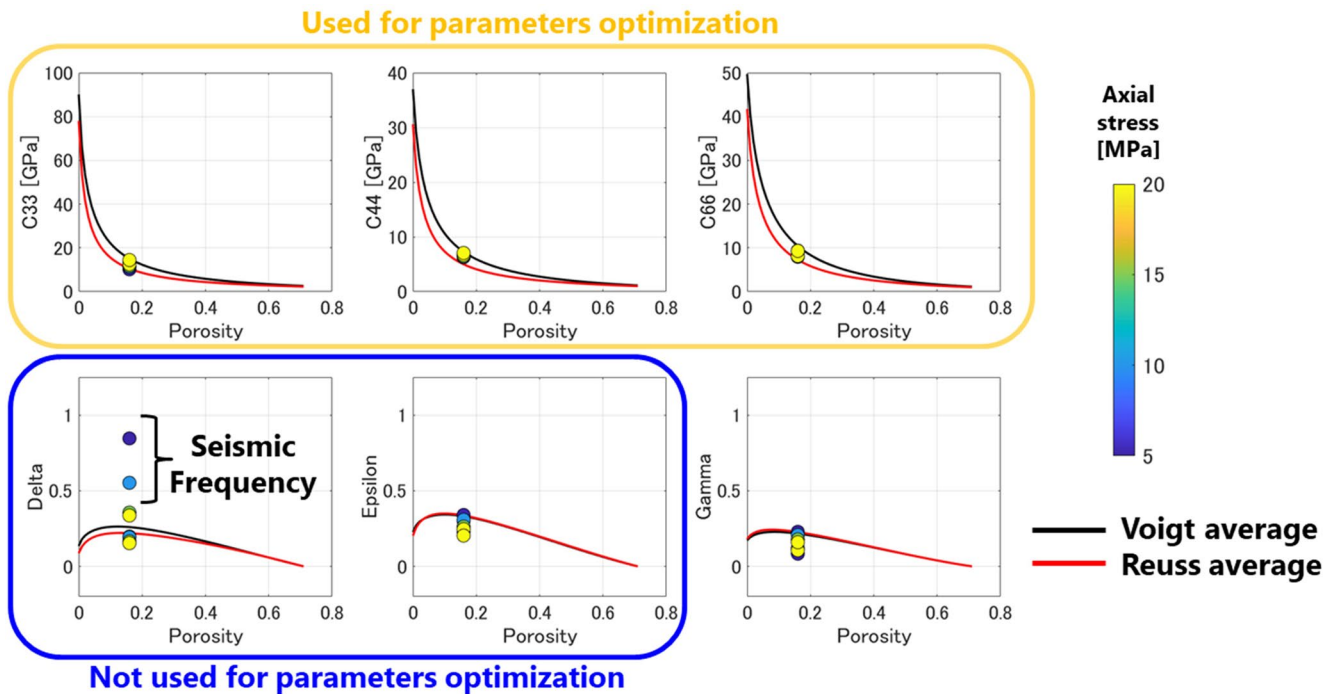
Figure 15. A comparison between optimized model (solid lines) and measurements (circle) on Pierre shale with water saturation of 0.23 provided by Szewczyk et al. (2018). Note that two different measurement results are shown; (1) measurements at seismic frequencies obtained by forced deformation method and (2) measurements at ultrasonic frequencies.
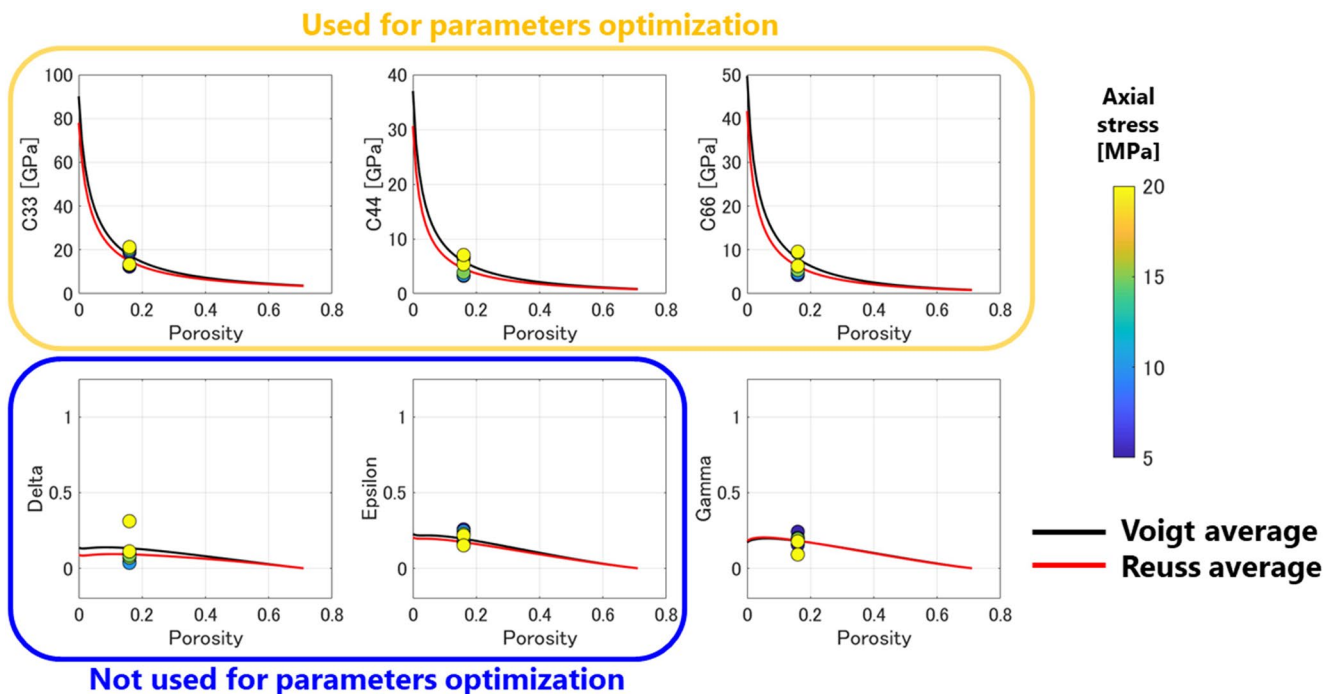

Figure 16. A comparison between optimized model (solid lines) and measurements (circle) on Pierre shale with water saturation of 0.7 provided by Szewczyk et al. (2018). Note that two different measurement results are shown; (1) measurements at seismic frequencies obtained by forced deformation method and (2) measurements at ultrasonic frequencies.
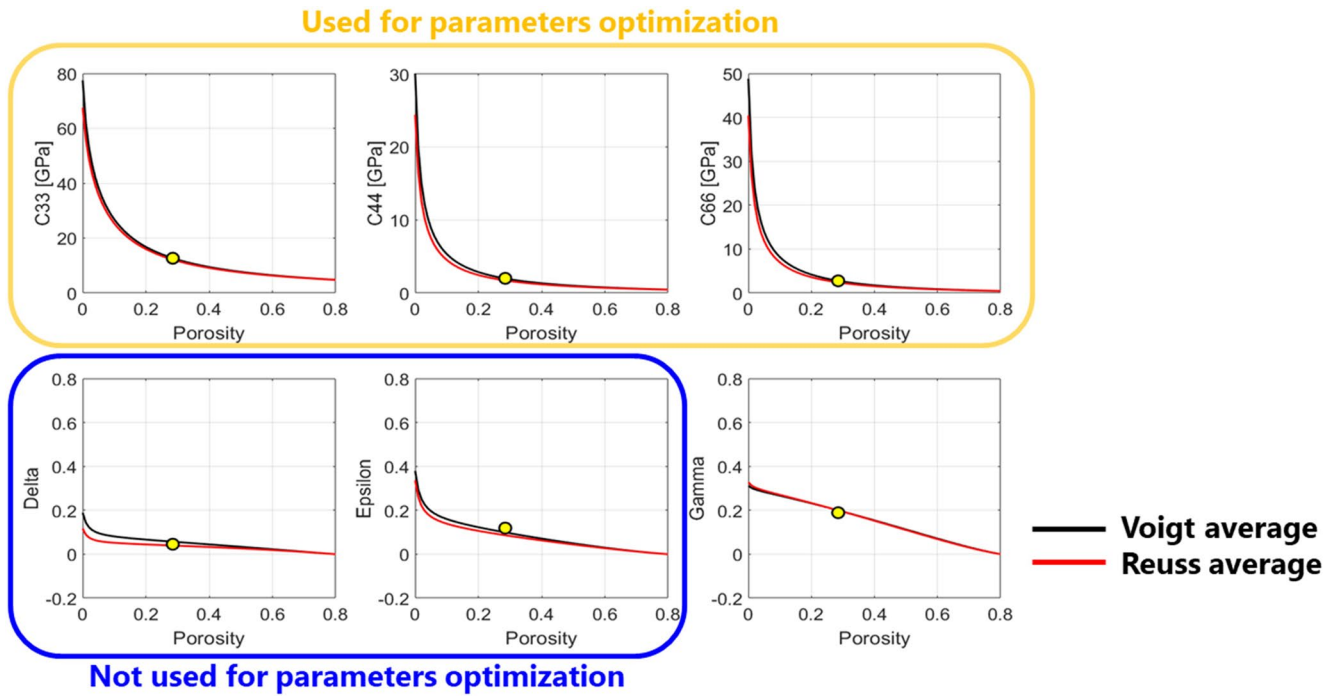
Figure 17. A comparison between optimized model (solid lines) and measurements (circle) on D2 shale sample provided by SINTEF Industry AS.
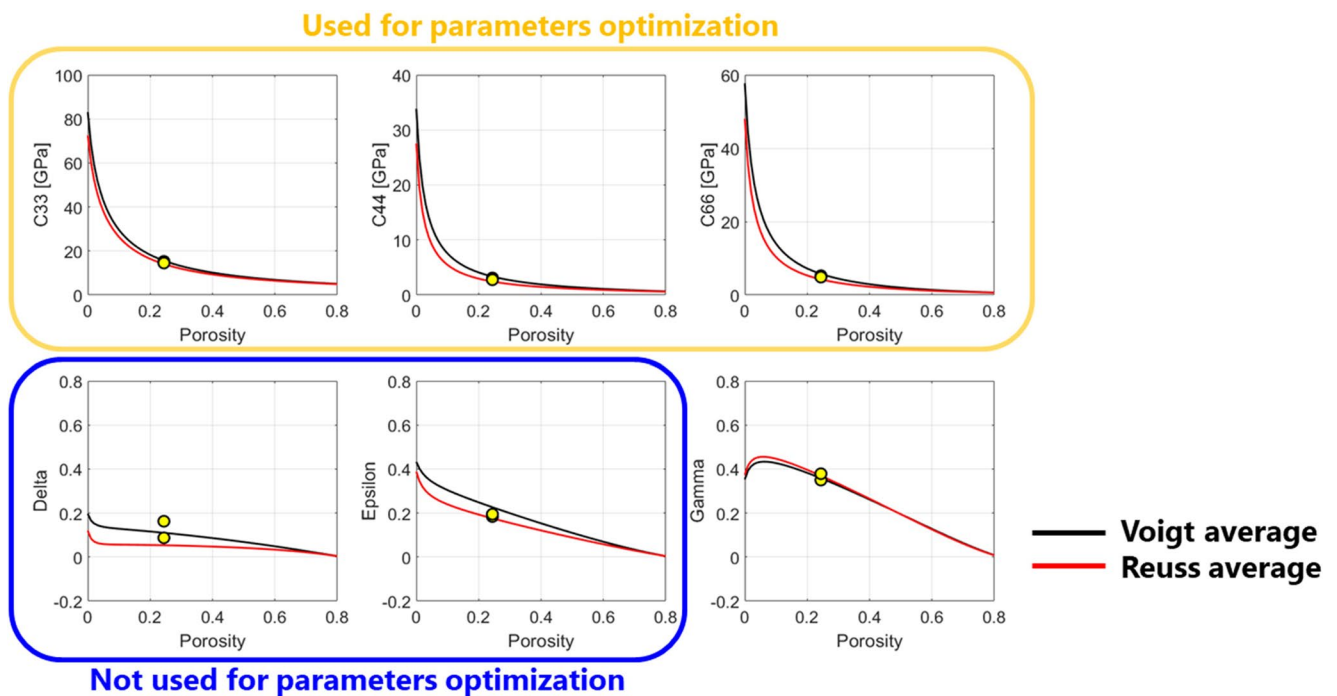

Figure 18. A comparison between optimized model (solid lines) and measurements (circle) on B3 shale sample at two different temperatures provided by SINTEF Industry AS.

Hofmann (2006), Norwegian Sea shale sample provided by Dewhurst et al. (2011), Mancos shale sample provided by Sarker and Batzle (2010), Opalinus Clay sample ("Shaly facies 3") provided by Lozovyi and Bauer (2019), Pierre shale sample with water saturation of 0.23 provided by Szewczyk et al. (2018), Pierre shale sample with water saturation of 0.7 provided by Szewczyk et al. (2018), D2 shale, and B3 shale provided by SINTEF, respectively. Interesting findings are as follows:

1. Most of modeled anisotropy parameters δ and ε are consistent with the measured values despite the fact that C_{11} and C_{13} were not used for the model parameters optimization.
2. Interplatelet medium bulk modulus optimized for Jurassic shale, Norwegian Sea shale, Shaly facies 3, Shaly facies 4, Sandy facies 2, D2 shale, and B3 shale, all saturated with water or brine, are similar to that of brine. On the other hand, those optimized for Kimmeridge shale and shale 2 are smaller than that of brine, despite the fact that those samples are saturated with water or brine (note that the grid search with the bulk modulus of brine did not give reasonable results for these samples).
3. Low interplatelet bulk modulus derived for Mancos shale seems to be consistent with the fact that the sample is saturated with decane.
4. Interplatelet medium bulk modulus optimized for Pierre shale increases with an increase in water saturation.
5. For fully brine or water saturated samples, optimized interplatelet medium shear modulus is much smaller than interplatelet medium bulk modulus. This is consistent with aforementioned inversion results by Sayers and den Boer (2018) and discrete-element modeling results by Holt and Kolstø (2017).

The observation that modeled anisotropy parameters δ and ε are consistent with the measured values indicates that the model could be used to predict those parameters using available information obtained by sonic tools. Moreover, it seems that optimized interplatelet medium properties are reasonable for most of samples, implying the correctness of the model.

5. Discussion

5.1. Assumptions

Assumptions made in the modeling will be discussed here. First, clay platelets are assumed to consist of muscovite or ideal kaolinite, whose properties are based on the best-fitting TI approximation of theoretical calculations of Militzer et al. (2011). Muscovite properties were used for most of samples since muscovite is both structurally and compositionally similar to the clay mineral illite, thus may be expected to have similar elastic properties (Katahara, 1996; Sayers & den Boer, 2019; Tosaya, 1982), while ideal kaolinite properties were used for Norwegian Sea shale because it is dominated by kaolinite. Although the assumption gave reasonable results, actual clay mineral properties, which have not been measured experimentally, might be largely different from the theoretical calculations, and clay platelets could actually consist of multiple minerals (or there may be domains of different clay minerals).

Second, it is assumed that the impact of diagenesis can be accounted for by the manual adjustment of initial porosity (orientation distribution) and changes in mineralogy and other model parameters (clay platelet aspect ratio, interplatelet medium properties, and the porosity). At temperatures larger than ~60°C–80°C smectite clay reacts with K-feldspar to form illite and quartz (Bjørlykke, 1998; Bjørlykke & Aagaard, 1992; Peltonen et al., 2008). Similarly, at temperature larger than 130°C–140°C, kaolinite reacts with K-feldspar to form illite (Bjørlykke, 1998; Bjørlykke & Aagaard, 1992). These reactions affect elastic properties of shales through: (a) dehydration (both reactions release water): dehydration of clay minerals increases the porosity due to partial phase changes from solid to fluid and could contribute to overpressure build-up (Bjørlykke, 1998; Bjørlykke & Aagaard, 1992), (b) changes in mineralogy, (c) changes in the orientation of the particles: for example, illite platelets may be precipitated with a preferential horizontal orientation (e.g., Ho et al., 1999), and (d) connection of grains: the precipitation of minerals (cements) will bind grains together. Changes in pore size and pore pressure caused by dehydration can be accounted for by the porosity and interplatelet medium properties (bulk modulus and shear modulus). Mineralogy can be easily modified. The orientation changes caused by illite precipitation can be taken into account by the manual adjustment of initial porosity. Connection of grains could be modeled by increasing the clay platelet aspect ratio. These adjustments, however, may not be enough in some cases. For example, if the precipitation of minerals
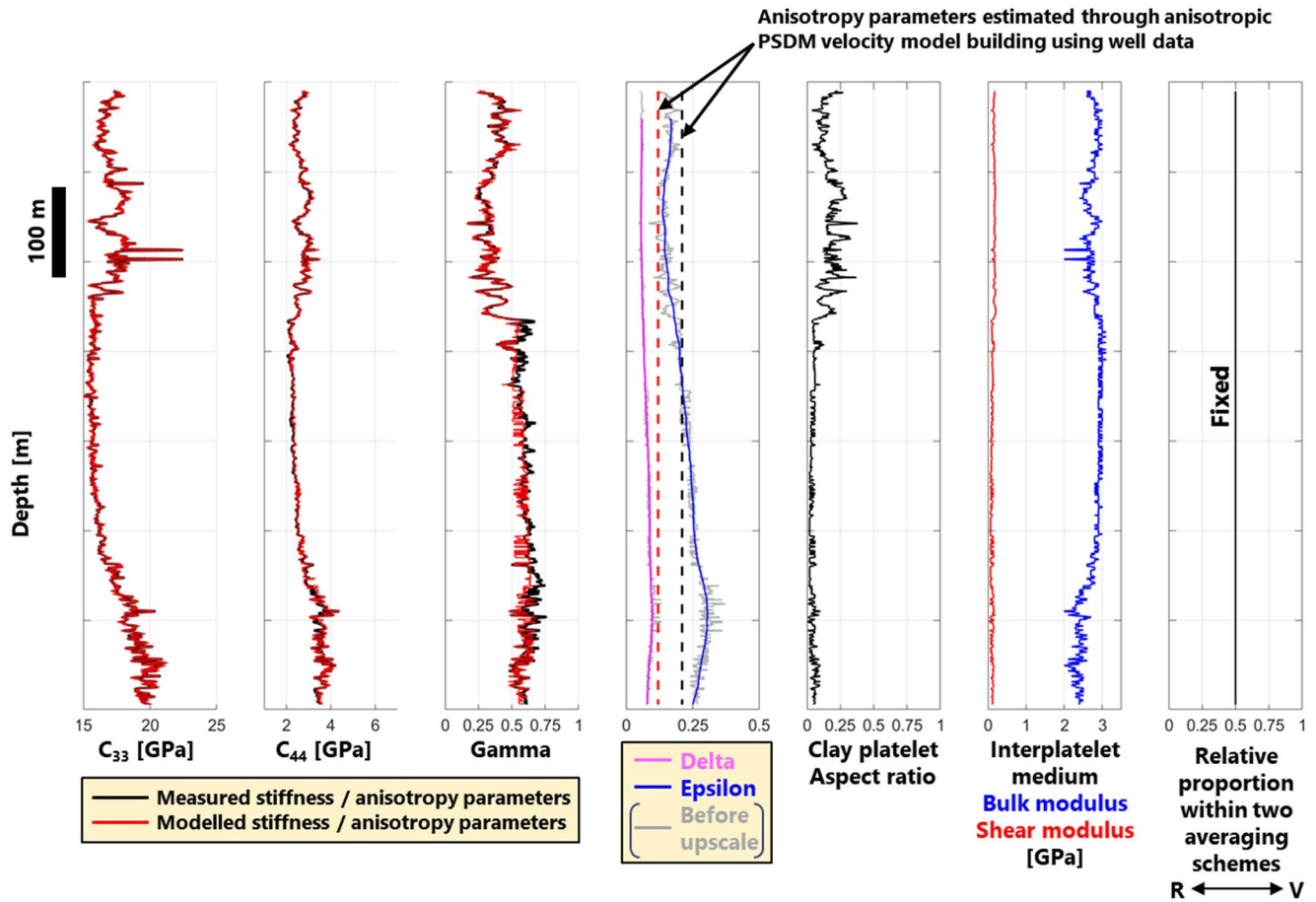
Figure 19. Results of anisotropy parameters (δ and ε) estimation from stiffnesses obtained by sonic tools in an offshore Western Australia field.

bridges the pores where domains consist of interconnected clay platelets and pore space, the lower anisotropic Hashin-Shtrikman estimates are not applicable since the most compliant phase is utilized as the matrix (it therefore gives a strict lower bound). Rock physics models for discrete inclusions in a shale matrix are appropriate in this case. The upper Hashin-Shtrikman estimates, where the matrix is the stiffest phase, or the aforementioned extended Maxwell's homogenization scheme used in the step 3 can be adopted. Other possible approaches include the model proposed by Dræge et al. (2006) in which the self-consistent approach and differential effective medium theory are utilized to model cemented shales. Moreover, the orientation of the particles after the chemical reactions may not be handled by the compaction ODF. The compaction ODF enforces a relation between W_{200} and W_{400}, but different types of orientation distribution can be obtained by varying W_{400} for a given W_{200} as demonstrated by Sayers (1994). Note that the anellilpticity depends on W_{400} (Sayers, 1994), and the enforced relation between W_{200} and W_{400} therefore results in constrained anellipticity.

Furthermore, secondary factors such as compliant porosity and bedding parallel cracks (e.g., Sayers, 2013a; Sayers & den Boer, 2019) were assumed to be insignificant and ignored here. Including such additional features may lead to better model predictions. The impact of the aforementioned assumption that the two-point correlation function defining the spatial distribution of clay platelets in the domains has the same aspect ratio as the clay platelets may not be negligible in some cases and has to be investigated in future work. The small bulk modulus obtained for Kimmeridge shale and shale 2 might be caused by the assumptions mentioned here. On the other hand, incomplete saturation cannot be completely ruled out, although efforts were made to completely saturate these samples.
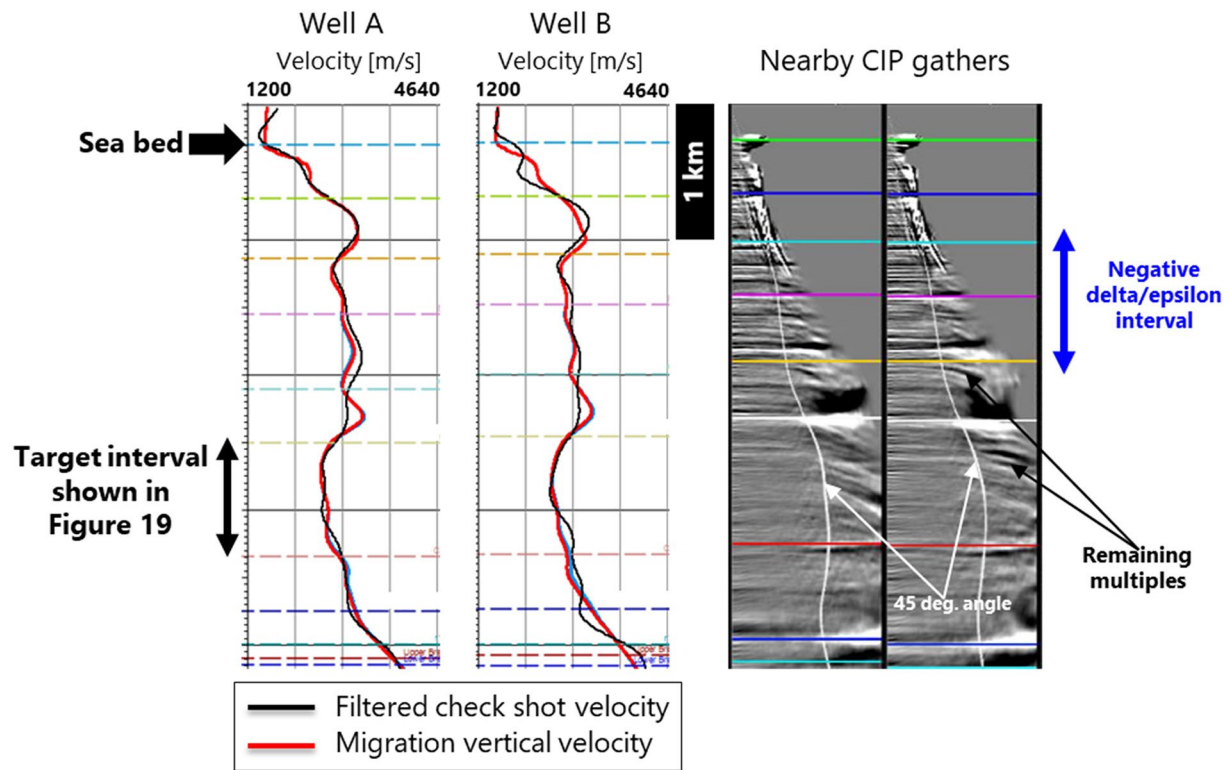
Figure 20. A comparison between migration velocity and check shot velocity. Nearby CIP gathers are shown on the right.

5.2. Implications

As mentioned earlier, the model parameters optimized based on measured C_{33}, C_{44}, and C_{66} gave reasonable estimates of δ and ε. C_{33} and C_{44} can be estimated from vertical P- and S-velocities and density, and C_{66} can be estimated from the Stoneley wave velocity measured by sonic tools (Norris & Sinha, 1993). The method can therefore be applied to data acquired in a vertical well. Figure 19 shows results of the application to a vertical well from an offshore Western Australia field in which C_{66} was estimated from the Stoneley wave velocity. Target interval, corresponding to Cretaceous age, mainly consists of claystone or calcareous claystone, and depositional environment is interpreted as distal shelf. Porosity was estimated from vertical P-wave velocity using empirical equation which is based on data from surrounding wells and curve fitting to it. Shale content was assumed to be 0.8 (quartz content of 0.2) based on information from surrounding wells. The initial porosity was calculated from the shale content using Equation 5. The grid search was performed to minimize the same normalized fit error in Equation 7. Note that the relative proportion of two averaging schemes are fixed at 0.5 since it gave almost the same results as that obtained by using the parameter as a free parameter. Combined with the fact that the relative proportion is only important for small clay platelet aspect ratio, fixing the parameter at 0.5 appears to be a reasonable approach in many cases. Fewer parameters need to be searched in this case. As shown in Figure 19, measured stiffnesses (C_{33} and C_{44}) and anisotropy parameter γ, which is a function of C_{44} and C_{66}, are reasonably explained by the model. Estimated fluid bulk modulus in this interval, based on Batzle and Wang equation (Batzle & Wang, 1992), is about 2.6 GPa. The optimized interplatelet medium bulk modulus is more or less consistent with this value. The optimized interplatelet medium shear modulus is about 0.05–0.2 GPa, and similar to some of shale samples investigated earlier and field data observations by Gelinsky (2020). Interestingly, predicted anisotropy parameters δ and ε are consistent with those estimated through anisotropic PSDM velocity model building using well data (shown by dashed lines in the fourth track in Figure 19), indicating that the prediction is reasonable. As mentioned earlier, low-resolution anisotropy parameters are utilized for seismic imaging. Anisotropic Backus averaging (Mavko et al., 2009) with window length of about 60 m (corresponding to wavelength) was therefore performed to upscale the predicted high-resolution anisotropy

parameters. Note that the anisotropic PSDM velocity model update was performed by adopting workflow similar to that mentioned in Asaka et al. (2016); Thomsen's δ was determined by analyzing the difference between check-shot velocity with good quality and migration velocity and ε was determined by analyzing the far offset gather flatness. Because of simple overburden geology, fixed interval δ and ε pairs were used for a given layer. Depth and isochore errors, matching between check shot and migration velocities, and gather flatness were carefully monitored throughout the velocity model updates to generate reliable model. Final migration velocity gives reasonable gather flatness and it matches nicely with check shot velocity (Figure 20). The mean and standard derivation of isochore error at the interval shown in Figure 19, based on 12 wells, are less than 1 and 9 m, respectively. Predicted δ and ε therefore have a wide range of application including anisotropic AVO modeling, a prior information for anisotropic PSDM velocity model building and wellbore stability analysis.

5.3. Model Parameters Estimation Using Different Information

Input for the model parameters estimation has to be optimized depending on data availability and accuracy of measured velocities. For example, C_{66} is not always available and ultrasonic S-wave velocity measurements may contain large error. Model parameters optimization using different information will be briefly discussed here. Following input options were investigated using the Jurassic shale, the Norwegian Sea shale, B3 shale and D2 shale mentioned above: (a) C_{11} and C_{33}, (b) E_v and E_h, (c) C_{11}, C_{33}, and C_{44}, and (d) E_v, E_h, and ν_{vh}. Options (a) and (b) were investigated because those are the most accurate data from ultrasonic measurements and low frequency set-ups, respectively. Options (c) and (d) were investigated to see the impact of additional information. Options (a) and (b) gave unstable results, while reasonable results were obtained by options (c) and (d). The observations indicate that at least three independent elastic parameters are necessary to reasonably estimate model parameters.

6. Conclusions

A predictive rock physics model for shales was developed by combining existing theories. Domain properties are calculated using the Sayers and den Boer model and the effect of domain orientation is taken into account by the compaction ODF. The applicability of the model to existing core measurements was investigated. The main results can be summarized as follows:

1. Most of modeled anisotropy parameters δ and ε are consistent with the measured values despite the fact that C_{11} and C_{13} were not used for the model parameters optimization.
2. Most of optimized interplatelet medium bulk modulus are consistent with the saturated fluid (a few inconsistent results might be caused by the assumptions made in the modeling, or possibly due to incomplete saturation).
3. For fully brine or water saturated samples, optimized interplatelet medium shear modulus is much smaller than the interplatelet medium bulk modulus. This is supported by existing studies.

These findings indicate the correctness of the model and that it could be used to predict anisotropy parameters from limited information, with the assumptions in mind. The application to a vertical well with the Stoneley wave velocity measurement gave reasonably estimated anisotropy parameters δ and ε. Predicted anisotropy parameters have a wide range of application including anisotropic AVO modeling, a prior information for anisotropic PSDM velocity model building and wellbore stability analysis.

Appendix A: Voigt and Reuss Approximations

Using the two coefficients in an expression of the orientation distribution function in generalized spherical harmonics, W_{200} and W_{400}, the Voigt approximation and the Reuss approximation can be performed. Voigt stiffness tensor of a TI aggregate is given by Sayers (1994):

$$C_{11} = C_{11}^{iso} + \frac{4\sqrt{2}}{105}\pi^2\left(2\sqrt{5}a_3 W_{200} + 3a_1 W_{400}\right)$$

$$C_{33} = C_{33}^{iso} - \frac{16\sqrt{2}}{105}\pi^2\left(\sqrt{5}a_3 W_{200} - 2a_1 W_{400}\right)$$

$$C_{13} = C_{13}^{iso} + \frac{4\sqrt{2}}{315}\pi^2\left\{\sqrt{5}\left(7a_2 - a_3\right)W_{200} - 12a_1 W_{400}\right\}$$

$$C_{44} = C_{44}^{iso} - \frac{2\sqrt{2}}{315}\pi^2\left\{\sqrt{5}\left(7a_2 + 2a_3\right)W_{200} + 24a_1 W_{400}\right\} \tag{A1}$$

$$C_{66} = C_{66}^{iso} + \frac{4\sqrt{2}}{315}\pi^2\left\{\sqrt{5}\left(7a_2 + 2a_3\right)W_{200} + 4a_1 W_{400}\right\}$$

$$C_{12} = C_{11} - 2C_{66}$$

where,

$$a_1 = C_{11}^a + C_{33}^a - 2C_{13}^a - 4C_{44}^a$$

$$a_2 = C_{11}^a - 3C_{12}^a + 2C_{13}^a - 2C_{44}^a$$

$$a_3 = 4C_{11}^a - 3C_{33}^a - C_{13}^a - 2C_{44}^a$$

$$C_{11}^{iso} = C_{33}^{iso} = \frac{1}{15}\left(8C_{11}^a + 3C_{33}^a + 4C_{13}^a + 8C_{44}^a\right)$$

$$C_{13}^{iso} = \frac{1}{15}\left(C_{11}^a + C_{33}^a + 5C_{12}^a + 8C_{13}^a - 4C_{44}^a\right) \tag{A2}$$

$$C_{44}^{iso} = \frac{1}{30}\left(7C_{11}^a + 2C_{33}^a - 5C_{12}^a - 4C_{13}^a + 12C_{44}^a\right)$$

$$C_{66}^{iso} = \frac{1}{15}\left(C_{11}^a + C_{33}^a - 2C_{13}^a + 6C_{44}^a + 5C_{66}^a\right)$$

Superscript "a" denotes the stiffness of the domain. Reuss compliance tensor of an aggregate is given by Sayers (1987):

$$S_{11} = S_{11}^{iso} + \frac{4\sqrt{2}}{105}\pi^2\left(2\sqrt{5}s_3 W_{200} + 3s_1 W_{400}\right)$$

$$S_{33} = S_{33}^{iso} - \frac{16\sqrt{2}}{105}\pi^2\left(\sqrt{5}s_3 W_{200} - 2s_1 W_{400}\right)$$

$$S_{13} = S_{13}^{iso} + \frac{4\sqrt{2}}{315}\pi^2\left\{\sqrt{5}\left(7s_2 - s_3\right)W_{200} - 12s_1 W_{400}\right\}$$

$$S_{44} = S_{44}^{iso} - \frac{8\sqrt{2}}{315}\pi^2\left\{\sqrt{5}\left(7s_2 + 2s_3\right)W_{200} + 24s_1 W_{400}\right\} \tag{A3}$$

$$S_{66} = S_{66}^{iso} + \frac{16\sqrt{2}}{315}\pi^2\left\{\sqrt{5}\left(7s_2 + 2s_3\right)W_{200} + 3s_1 W_{400}\right\}$$

$$S_{12} = S_{11} - \frac{S_{66}}{2}$$

where,

$$s_1 = S_{11}^a + S_{33}^a - 2S_{13}^a - S_{44}^a$$

$$s_2 = S_{11}^a - 3S_{12}^a + 2S_{13}^a - \frac{S_{44}^a}{2}$$

$$s_3 = 4S_{11}^a - 3S_{33}^a - S_{13}^a - \frac{S_{44}^a}{2}$$

$$S_{11}^{iso} = S_{33}^{iso} = \frac{1}{15}\left(8S_{11}^a + 3S_{33}^a + 4S_{13}^a + 2S_{44}^a\right)$$

$$S_{13}^{iso} = \frac{1}{15}\left(S_{11}^a + S_{33}^a + 5S_{12}^a + 8S_{13}^a - S_{44}^a\right) \tag{A4}$$

$$S_{44}^{iso} = \frac{2}{15}\left(7S_{11}^a + 2S_{33}^a - 5S_{12}^a - 4S_{13}^a + 3S_{44}^a\right)$$

$$S_{66}^{iso} = \frac{1}{15}\left(4S_{11}^a + 4S_{33}^a - 8S_{13}^a + 6S_{44}^a + 5S_{66}^a\right)$$

See Morris (1969) for the basis of this approach. Verification of the approximations calculation was performed by reproducing the results of Sayers (2005).

Data Availability Statement

The experimental data used in this paper can be obtained as follows: Jurassic shale: Measured elastic properties were obtained from *Mr. Anisotropy* database complied by Horne (2013). The database is available on request by sending an email to Mr.Anisotropy@gmail.com. Mineralogy is listed in Table 1 and porosity is shown in Figure 3 in Hornby (1998). Kimmeridge shale: Measured elastic properties were obtained from *Mr. Anisotropy* database. Mineralogy is listed in Table 2 and porosity is mentioned in section 3.1 in Hornby (1998). Shale 2: Measured elastic properties were obtained from *Mr. Anisotropy* database. Mineralogy is listed in Table 3.3 and porosity is mentioned in section 3.3.1 in Hofmann (2006). Norwegian sea shale: Measured elastic properties were obtained from *Mr. Anisotropy* database. Mineralogy and porosity are listed in Table 1 and Table 4 in Dewhurst et al. (2011), respectively. Mancos shale: Measured elastic properties were obtained from *Mr. Anisotropy* database. Mineralogy and porosity are mentioned in section "Sample Description" in Sarker and Batzle (2010). Opalinus Clay: Measured static undrained stiffness parameters are listed in column 7–11 of Table 5 and Table 6, zero-stress extrapolated static undrained stiffness parameters are listed in column 7–11 of Table 7 and Table 8, and dynamic stiffness parameters at ultrasonic frequency are listed in column 9–13 of Table 9 in Lozovyi and Bauer (2019). Mineralogy is listed in Table 1 while porosities are mentioned in section 2.1 in Lozovyi and Bauer (2019). Pierre shale: Measured elastic properties are listed in Table 4 while mineralogy and porosity are mentioned in section 2.1 in Szewczyk et al. (2019). D2, B3, and B4 shales: Restrictions apply to the general availability of the Data from SINTEF that support the results of this study (D2, B3, and B4 shales), which were generated under the projects "Improved prediction of stress and pore-pressure changes in the overburden for infill drilling" (Norwegian Research Council Grant 294369) and "Shale Rock Physics: Improved Seismic Monitoring for Increased Recovery Consortium" (Norwegian Research Council Grant 234074). Data are available from SINTEF AS, by its research institute SINTEF Industry, subject to the permissions of the owners of the data. Key features of the Data are published in Holt et al. (Geophysics, 2018, https://doi.org/10.1190/geo2017-0652.1).

References

Antognozzi, M., Humphris, A. D. L., & Miles, M. J. (2001). Observation of molecular layering in a confined water film and study of the layers viscoelastic properties. *Applied Physics Letters*, *78*, 300–302. https://doi.org/10.1063/1.1339997

Asaka, M., Sekine, T., & Furuya, K. (2016). Geologic cause of seismic anisotropy: A case study from offshore Western Australia. *The Leading Edge*, *35*(8), 662–668. https://doi.org/10.1190/tle35080662.1

Aylmore, L. A. G., & Quirk, J. P. (1960). Domain or turbostratic structure of clays. *Nature*, *187*(4742), 1046–1048. https://doi.org/10.1038/1871046a0

Backus, G. E. (1962). Long-wave elastic anisotropy produced by horizontal layering. *Journal of Geophysical Research*, *67*, 4427–4440. https://doi.org/10.1029/JZ067i011p04427

Baker, D. W., Chawla, K. S., & Krizek, R. J. (1993). Compaction fabrics of pelites: Experimental consolidation of kaolinite and implications for analysis of strain in slate. *Journal of Structural Geology*, *15*, 1123–1137. https://doi.org/10.1016/0191-8141(93)90159-8

Bakk, A., Fjær, E., & Holt, R. M. (2006). *Simple model for lithological anisotropy of shale*. 68th Conference and Exhibition, EAGE, Extended Abstracts. https://doi.org/10.3997/2214-4609.201402297

Bakk, A., Holt, R. M., Bauer, A., Dupuy, B., & Romdhane, A. (2020). Offset dependence of overburden time-shifts from ultrasonic data. *Geophysical Prospecting*, *68*, 1847–1863. https://doi.org/10.1111/1365-2478.12963

Bandyopadhyay, K. (2009). *Seismic anisotropy: Geological causes and its implications to reservoir geophysics* (PhD dissertation). Stanford University.

Batzle, M., Han, D.-H., & Hofmann, R. (2006). Fluid mobility and frequency-dependent seismic velocity—Direct measurements. *Geophysics*, *71*(1), N1–N9. https://doi.org/10.1190/1.2159053

Batzle, M., & Wang, Z. (1992). Seismic properties of pore fluids. *Geophysics*, *57*, 1396–1408. https://doi.org/10.1190/1.1443207

Bayuk, I. O., Gay, J. K., Hooper, J. M., & Chesnokov, E. M. (2008). Upper and lower stiffness bounds for porous anisotropic rocks. *Geophysical Journal International*, *175*, 1309–1320. https://doi.org/10.1111/j.1365-246X.2008.03925.x

Bjørlykke, K. (1998). Clay mineral diagenesis in sedimentary basins—A key to the prediction of rock properties. Examples from the Noth Sea Basin. *Clay Minerals*, *33*, 15–34. https://doi.org/10.1180/000985598545390

Bjørlykke, K., & Aagaard, P. (1992). Clay minerals in North Sea sandstones. In *Origin, diagenesis, and petrophysics of clay minerals in sandstones* (pp. 65–80). SEPM. https://doi.org/10.2110/pec.92.47.0065

Blangy, J. P. (1994). AVO in transversely isotropic media—An overview. *Geophysics*, *59*(5), 775–781. https://doi.org/10.1190/1.1443635

Chichinina, T., & Vernik, L. (2018). Physical bounds on C13 and δ for organic mudrocks. *Geophysics*, *83*(5), A75–A79. https://doi.org/10.1190/GEO2018-0035.1

Dellinger, J., & Vernik, L. (1994). Do traveltimes in pulse-transmission experiments yield anisotropic group or phase velocities? *Geophysics*, *59*(11), 1774–1779. https://doi.org/10.1190/1.1443564

Dewhurst, D. N., & Siggins, A. F. (2006). Impact of fabric, microcracks and stress field on shale anisotropy. *Geophysical Journal International*, *165*, 135–148. https://doi.org/10.1111/j.1365-246X.2006.02834.x

Dewhurst, D. N., Siggins, A. F., Sarout, J., Raven, M. D., & Nordgård-Bolås, H. M. (2011). Geomechanical and ultrasonic characterization of a Norwegian Sea shale. *Geophysics*, *76*(3), WA101–WA111. https://doi.org/10.1190/1.3569599

Dræge, A., Jakobsen, M., & Johansen, T. A. (2006). Rock physics modelling of shale diagenesis. *Petroleum Geoscience*, *12*, 49–57. https://doi.org/10.1144/1354-079305-665

Dutta, P. (2018). *Microgeometry induced non-uniqueness in the elastic and electrical properties of rocks* (PhD dissertation). Stanford University.

Fjær, E., Holt, R. M., Horsrud, P., Raaen, A. M., & Risnes, R. (2008). *Petroleum related rock mechanics* (2nd ed., p. 491). Elsevier.

Fjær, E., Lothe, A. E., & Sylta, Ø. (2006). *Porosity versus depth relationship derived from rock mechanical arguments*. Poster on AAPG Conference.

Gassmann, F. (1951). Uber die Elastizität Poröser Medien. In M. A. Pelissier (Ed.), *Classics of elastic wave theory* Vol. (96, pp. 1–23). Vierteljahresschrift der Naturforschenden Gesellschaft in Zürich, SEG. (Translated as: On elasticity of porous media). https://doi.org/10.1190/1.9781560801931.ch3p

Gelinsky, S. (2020). *Reservoir characterization supported by rock physics diagnostics*. Paper presented at the Offshore Technology Conference Asia. https://doi.org/10.4043/30359-MS

Herwanger, J. V., & Horne, S. A. (2009). Linking reservoir geomechanics and time-lapse seismics: Predicting anisotropic velocity changes and seismic attributes. *Geophysics*, *74*(4), W13–W33. https://doi.org/10.1190/1.3122407

Ho, N.-C., Peacor, D. R., & van der Pluijm, B. A. (1999). Preferred orientation of phyllosilicates in Gulf Coast mudstones and relation to the smectite-illite transition. *Clays and Clay Minerals*, *47*(4), 495–504. https://doi.org/10.1346/CCMN.1999.0470412

Hofmann, R. (2006). *Frequency dependent elastic and anelastic properties of clastic rocks* (PhD dissertation). Colorado School of Mines.

Holt, R. M. (2016). Bounds of elastic parameters characterizing transversely isotropic media: Application to shales. *Geophysics*, *81*(5), C243–C252. https://doi.org/10.1190/GEO2015-0485.1

Holt, R. M., & Fjær, E. (2003). *Wave velocities in shales—A rock physics model*. 65th Conference and Exhibition, EAGE, Extended Abstracts. https://doi.org/10.3997/2214-4609-pdb.6.C13

Holt, R. M., & Kolstø, M. I. (2017). How does water near clay mineral surfaces influence the rock physics of shale? *Geophysical Prospecting*, *65*, 1615–1629. https://doi.org/10.1111/1365-2478.12503

Hornby, B. E. (1998). Experimental laboratory determination of the dynamic elastic properties of wet, drained shales. *Journal of Geophysical Research*, *103*(B12), 29945–29964. https://doi.org/10.1029/97JB02380

Hornby, B. E., Schwartz, L. M., & Hudson, J. (1994). Anisotropic effective-medium modelling of the elastic properties of shales. *Geophysics*, *59*, 1570–1583. https://doi.org/10.1190/1.1443546

Horne, S. A. (2013). A statistical review of mudrock elastic anisotropy. *Geophysical Prospecting*, *61*, 817–826. https://doi.org/10.1111/1365-2478.12036

Johansen, T. A., Ruud, B. O., & Jakobsen, M. (2004). Effect of grain scale alignment on seismic anisotropy and reflectivity of shales. *Geophysical Prospecting*, *52*, 133–149. https://doi.org/10.1046/j.1365-2478.2003.00405.x

Katahara, K. W. (1996). *Clay mineral elastic properties* (pp. 1691–1694). 66th SEG meeting, Expanded Abstracts. https://doi.org/10.1190/1.1826454

Lin, R., & Thomsen, L. (2013). *Extracting polar anisotropy parameters from seismic data and well logs* (pp. 310–314). 83th SEG meeting. Expanded Abstracts. https://doi.org/10.1190/segam2013-1150.1

Lozovyi, S., & Bauer, A. (2019). Static and dynamic stiffness measurements with Opalinus Clay. *Geophysical Proepecting*, *67*, 997–1019. https://doi.org/10.1111/1365-2478.12720

Major, R. C., Houston, J. E., McGrath, M. J., Siepmann, J. I., & Zhu, X.-Y. (2006). Viscous water meniscus under nanoconfinement. *Physical Review Letters*, *96*, 177803. https://doi.org/10.1103/PhysRevLett.96.177803

Mavko, G., & Bandyopadhyay, K. (2009). Approximate fluid substitution for vertical velocities in weakly anisotropic VTI rocks. *Geophysics*, *74*(1), D1–D6. https://doi.org/10.1190/1.3026552

Mavko, G., Mukerji, T., & Dvorkin, J. (2009). *The rock physics handbook* (2nd ed.). Cambridge University Press.

Maxwell, J. C. (1873). *A treatise on electricity and magnetism*. Clarendon Press.

Mikhaltsevitch, V., Lebedev, M., Pervukhina, M., & Gurevich, B. (2021). Seismic dispersion and attenuation in Mancos shale—Laboratory measurements. *Geophysical Prospecting*, *69*, 568–585. https://doi.org/10.1111/1365-2478.13056

Militzer, B., Wenk, H.-R., Stackhouse, S., & Stixrude, L. (2011). First-principles calculation of the elastic moduli of sheet silicates and their application to shale anisotropy. *American Mineralogist*, *96*, 125–137. https://doi.org/10.2138/am.2011.3558

Morris, P. R. (1969). Averaging fourth-rank tensors with weight functions. *Journal of Applied Physics*, *40*, 447–448. https://doi.org/10.1063/1.1657417

Norris, A. N., & Sinha, B. K. (1993). Weak elastic anisotropy and the tube wave. *Geophysics*, *58*(8), 1091–1098. https://doi.org/10.1190/1.1443493

Ortega, J. A., Ulm, F.-J., & Abousleiman, Y. (2007). The effect of the nanogranular nature of shale on their poroelastic behavior. *Acta Geotechnica*, *2*, 155–182. https://doi.org/10.1007/s11440-007-0038-8

Owens, W. H. (1973). Strain modification of angular density distributions. *Tectonophysics*, *16*, 249–261. https://doi.org/10.1016/0040-1951(73)90014-0

Peltonen, C., Marcussen, Ø., Bjørlykke, K., & Jahren, J. (2008). Mineralogical control on mudstone compaction: A study of Late Cretaceous to Early Tertiary mudstones of the Vøring and Møre basins, Norwegian Sea. *Petroleum Geoscience*, *14*, 127–138. https://doi.org/10.1144/1354-079308-758

Ponte Castaneda, P., & Willis, J. R. (1995). The effect of spatial distribution on the effective behavior of composite materials and cracked media. *Journal of the Mechanics and Physics of Solids*, *43*, 1919–1951. https://doi.org/10.1016/0022-5096(95)00058-Q

Roe, R. J. (1965). Description of crystallite orientation in polycrystalline materials, III, General solution to pole figure inversion. *Journal of Applied Physics*, *36*, 2024–2031. https://doi.org/10.1063/1.1714396

Ruud, B. O., Jakobsen, M., & Johansen, T. A. (2003). *Seismic properties of shales during compaction* (pp. 1294–1297). SEG Technical Program Expanded Abstracts. https://doi.org/10.1190/1.1817522

Sarker, R., & Batzle, M. (2010). *Anisotropic elastic moduli of the Mancos B shale—An experimental study* (pp. 2600–2605). SEG Technical Program Expanded Abstracts. https://doi.org/10.1190/1.3513381

Sayers, C. M. (1986). Angular dependent ultrasonic wave velocities in aggregates of hexagonal crystals. *Ultrasonics*, *24*, 289–291. https://doi.org/10.1016/0041-624X(86)90107-1

Sayers, C. M. (1987). The elastic anisotropy of polycrystalline aggregates of zirconium and its alloys. *Journal of Nuclear Materials*, *144*, 211–213. https://doi.org/10.1016/0022-3115(87)90033-X

Sayers, C. M. (1994). The elastic anisotropy of shales. *Journal of Geophysical Research*, *99*, 767–774. https://doi.org/10.1029/93JB02579

Sayers, C. M. (2005). Seismic anisotropy of shales. *Geophysical Prospecting*, *53*, 667–676. https://doi.org/10.1111/j.1365-2478.2005.00495.x

Sayers, C. M. (2013a). The effect of anisotropy on the Young's moduli and Poisson's ratios of shales. *Geophysical Prospecting*, *61*, 416–426. https://doi.org/10.1111/j.1365-2478.2012.01130.x

Sayers, C. M. (2013b). The effect of kerogen on the elastic anisotropy of organic-rich shales. *Geophysics*, *78*(2), D65–D74. https://doi.org/10.1190/GEO2012-0309.1

Sayers, C. M., & den Boer, L. D. (2016). The elastic anisotropy of clay minerals. *Geophysics*, *81*(5), C193–C203. https://doi.org/10.1190/GEO2016-0005.1

Sayers, C. M., & den Boer, L. D. (2018). The elastic properties of clay in shales. *Journal of Geophysical Research: Solid Earth*, *123*, 5965–5974. https://doi.org/10.1029/2018JB015600

Sayers, C. M., & den Boer, L. D. (2019). The impact of different clay minerals on the anisotropy of clay matrix in shale. *Geophysical Prospecting*, *67*, 2298–2318. https://doi.org/10.1111/1365-2478.12829

Sayers, C. M., & den Boer, L. D. (2020). Effect of variations in microstructure on clay elastic anisotropy. *Geophysics*, *85*(2), MR73–MR82. https://doi.org/10.1190/GEO2019-0374.1

Sevostianov, I. (2014). On the shape of effective inclusion in the Maxwell homogenization scheme for anisotropic elastic composites. *Mechanics of Materials*, *75*, 45–59. https://doi.org/10.1016/J.MECHMAT.2014.03.003

Sevostianov, I., & Giraud, A. (2013). Generalization of Maxwell homogenization scheme for elastic material containing inhomogeneities of diverse shape. *International Journal of Engineering Science*, *64*, 23–36. https://doi.org/10.1016/j.ijengsci.2012.12.004

Sevostianov, I., & Vernik, L. (2021). Micromechanics-based rock-physics model for inorganic shale. *Geophysics*, *86*(2), MR105–MR116. https://doi.org/10.1190/GEO2020-0500.1

Shumway, G. (1960). Sound speed and absorption studies of marine sediments by a resonance method. *Geophysics*, *25*, 451–467. https://doi.org/10.1190/1.1438717

Szewczyk, D., Bauer, A., & Holt, R. M. (2018). Stress-dependent elastic properties of shales-laboratory experiments at seismic and ultrasonic frequencies. *Geophysical Journal International*, *212*, 189–210. https://doi.org/10.1093/gji/ggx392

Thomsen, L. (1986). Weak elastic anisotropy. *Geophysics*, *51*(10), 1954–1966. https://doi.org/10.1190/1.1442051

Thomsen, L. (2014). *Seismic anisotropy in exploration and exploitation* (2nd ed.). The SEG/EAGE Distinguished Instructor Short Course #5 Lecture Notes, SEG.

Tosaya, C. A. (1982). *Acoustical properties of clay-bearing rocks* (PhD thesis). Stanford University.

Ulm, F.-J., & Abousleiman, Y. (2006). The nanogranular nature of shale. *Acta Geotechnica*, *1*, 77–88. https://doi.org/10.1007/s11440-006-0009-5

Vaughan, M. T., & Guggenheim, S. (1986). Elasticity of muscovite and its relationship to crystal structure. *Journal of Geophysical Research*, *91*, 4657–4665. https://doi.org/10.1029/JB091iB05p04657

Vernik, L. (2016). *Seismic petrophysics in quantitative interpretation*. SEG.

Vernik, L., & Anantharamu, V. (2020). Estimating the elastic properties of mica and clay minerals. *Geophysics*, *85*(2), MR83–MR95. https://doi.org/10.1190/GEO2018-0784.1

Vernik, L., & Kachanov, M. (2010). Modeling elastic properties of siliciclastic rocks. *Geophysics*, *75*(6), E171–E182. https://doi.org/10.1190/1.3494031

Vernik, L., & Landis, C. (1996). Elastic anisotropy of source rocks: Implications for hydrocarbon generation and primary migration. *AAPG Bulletin*, *80*(4), 531–544. https://doi.org/10.1306/64ed8836-1724-11d7-8645000102c1865d

Vernik, L., & Nur, A. (1992). Ultrasonic velocity and anisotropy of hydrocarbon source rocks. *Geophysics*, *57*(5), 727–735. https://doi.org/10.1190/1.1443286

Vilchevskaya, E., & Sevostianov, I. (2015). Effective elastic properties of a particulate composite with transversely-isotropic matrix. *International Journal of Engineering Science*, *94*, 139–149. https://doi.org/10.1016/j.ijengsci.2015.05.006

Wang, Z. (2002a). Seismic anisotropy in sedimentary rocks, part 1: A single-plug laboratory method. *Geophysics*, *67*(5), 1415–1422. https://doi.org/10.1190/1.1512787

Wang, Z. (2002b). Seismic anisotropy in sedimentary rocks, part 2: Laboratory data. *Geophysics*, *67*(5), 1423–1440. https://doi.org/10.1190/1.1512743

Willis, J. R. (1977). Bounds and self-consistent estimates for the overall properties of anisotropic composites. *Journal of the Mechanics and Physics of Solids*, *25*, 185–202. https://doi.org/10.1016/0022-5096(77)90022-9

Yan, F., Han, D.-H., & Chen, X.-L. (2018). Practical and robust experimental determination of c_{13} and Thomsen parameter δ. *Geophysical Prospecting*, *66*, 354–365. https://doi.org/10.1111/1365-2478.12514

Yan, F., Han, D.-H., & Yao, Q. (2016). Physical constraints on c_{13} and δ for transversely isotropic hydrocarbon source rocks. *Geophysical Prospecting*, *64*, 1524–1536. https://doi.org/10.1111/1365-2478.12265

Yurikov, A., Pervukhina, M., Beloborodov, R., Piane, C. D., Dewhurst, D. N., & Lebedev, M. (2021). Modeling of compaction trends of anisotropic elastic properties of shales. *Journal of Geophysical Research: Solid Earth*, *126*, 2020JB019725. https://doi.org/10.1029/2020JB019725